https://lib.uliege.be https://matheo.uliege.be

Development of CFD Simulations of Supersonic Jet Impingement on a Liquid Surface in the Electric Arc Furnace Université de Liège

Auteur : Mattson, Tyler
Promoteur(s) : Terrapon, Vincent
Faculté : Faculté des Sciences appliquées
Diplôme : Master en ingénieur civil en aérospatiale, à finalité spécialisée en "aerospace engineering"
Année académique : 2025-2026
URI/URL : http://hdl.handle.net/2268.2/26175

Avertissement à l'attention des usagers :

Tous les documents placés en accès ouvert sur le site le site MatheO sont protégés par le droit d'auteur. Conformément aux principes énoncés par la "Budapest Open Access Initiative"(BOAI, 2002), l'utilisateur du site peut lire, télécharger, copier, transmettre, imprimer, chercher ou faire un lien vers le texte intégral de ces documents, les disséquer pour les indexer, s'en servir de données pour un logiciel, ou s'en servir à toute autre fin légale (ou prévue par la réglementation relative au droit d'auteur). Toute utilisation du document à des fins commerciales est strictement interdite.

Par ailleurs, l'utilisateur s'engage à respecter les droits moraux de l'auteur, principalement le droit à l'intégrité de l'oeuvre et le droit de paternité et ce dans toute utilisation que l'utilisateur entreprend. Ainsi, à titre d'exemple, lorsqu'il reproduira un document par extrait ou dans son intégralité, l'utilisateur citera de manière complète les sources telles que mentionnées ci-dessus. Toute utilisation non explicitement autorisée ci-avant (telle que par exemple, la modification du document ou son résumé) nécessite l'autorisation préalable et expresse des auteurs ou de leurs ayants droit.

UNIVERSITE DE LIEGE
FACULTE DES SCIENCES APPLIQUEES

Development of CFD Simulations of Supersonic Jet Impingement on a Liquid Surface in the Electric Arc Furnace

Tyler MATTSON

Thesis presented to obtain the degree of:
Master of Science in Aerospace Engineering

Thesis supervisor:
Dr. Vincent TERRAPON

Academic year: **2025 - 2026**

Abstract

RANS-based CFD simulations of impinging gas jets onto liquid surfaces are conducted using the VOF method to study the jet-bath interaction in the Electric Arc Furnace steelmaking process. The VOF model is first validated using simplified air-water simulations, which are compared with experimental measurements and empirical correlations. The validation results show good agreement between the VOF simulation and experimental results for cavity properties and jet-induced flow. Bubbles are then represented using Lagrangian particles to emulate the production of bubbles from chemical reactions in the EAF process. The results show that bubble generation by gas-phase mass stripping at the cavity's surface increases the cavity depth while decreasing its radius. Finally, a simplified cold model representative of EAF blowing conditions is simulated using a standard supersonic jet. The resulting cavity response and flow in the bath are reported to provide a baseline for future comparison with coherent supersonic jets under EAF conditions.

Acknowledgments

I would like to thank my supervisor Professor Vincent Terrapon for all of his guidance, support and valuable feedback throughout the development of this thesis.

I would also like to thank Mars and Xavier for their help with the computational tools, and their support in developing the simulations.

Finally, I would like to express my sincere gratitude to my family and friends for their unconditional support throughout my studies.

Contents

List of Figures

List of Tables

Chapter 1

Industrial Context

As global energy and resource usage continues to climb, it is becoming ever more important to move towards more sustainable processes. Due to steel's ubiquitous usage in our modern world, developing a more efficient steelmaking process can make a sizable contribution to reducing energy and resource consumption.

The first step towards improving the efficiency of the steelmaking process is to develop a comprehensive understanding of the procedure as a whole. As knowledge on the process grows, inefficiencies in the method can be identified and improved.

1.1 The Steel Industry

Steel is an alloy composed mostly of iron and carbon, with other trace metals dispersed throughout the material at lower concentrations. The carbon content of steel is less than 2 %, and the concentration can be varied to provide the material with different properties. The other trace elements like manganese, silicon, phosphorus, sulfur and oxygen can also have their concentration manipulated to best tailor the steel for its ultimate purpose. [18]

This variation in composition allows different alloys of steel to be used for a wide range of applications, making it the most important engineering and construction material. In 2024, 1,885 million tonnes of crude steel was produced, and the value added from producing steel was estimated to be US $500 billion, based on 2017 data. If the total steel supply chain from raw material to finished product is considered, that value rises to US $2.9 trillion, which was equivalent to 3.9% of the global GDP in that year. This shows that steel is a huge part of the modern economy, and any improvements to the process can have a huge impact on a global scale. [19]

The large role that steel plays in the global economy also leads steel to be an important priority for sustainability efforts. In 2023 casting 1 tonne of crude steel produced 1.9 tonnes of CO_2. Scaling up to the global scale shows that in 2024 roughly 3.6 billion tonnes of CO_2 were produced directly through steel production, equivalent to roughly 9.2% of global emissions in that year. Improving the efficiency of the steelmaking process would be an immense step towards reducing global greenhouse gas emissions. [20]

1.2 Steel Production

There are two different methods that are widely used to create steel, the Blast Furnace-Basic Oxygen Furnace (BF-BOF) method, and the Electric Arc Furnace (EAF) method. They both work by melting bulk metal that is rich in iron, and introducing oxygen to the mixture to remove impurities in the metal, creating steel.

The BF-BOF method uses iron oxides as the iron supply, which is the form of iron mined from the crust of the earth. The oxygen in the iron oxide is removed by mixing the iron oxide with a coal-based fuel called "coke" at high temperatures in the blast furnace. At this elevated temperature the carbon in the coke reacts with the oxygen in the iron oxide to produce CO and CO_2. After the bulk of iron oxide is converted into iron, oxygen is blown onto the molten mixture to remove the excess carbon in a process called decarburization. The resulting mixture is virgin steel, and is then ready to be used for manufacturing.

The EAF method uses scrap steel or high-carbon "pig iron" as the iron supply, which is then melted by introducing a large electric current into the metal. Due to the fact that the iron already has a large carbon content, the coke-based heating process is avoided which allows the EAF method to use less than half of the energy of the BF-BOF method. Oxygen is then blown onto the molten mixture where it oxidizes with impurities in the metal, and decarburizes the bath. [21] [22]

An overview of the two methods is demonstrated in Figure 1.1, showing the differences between the materials required and processes used to refine the raw material to create the steel needed for the final product.

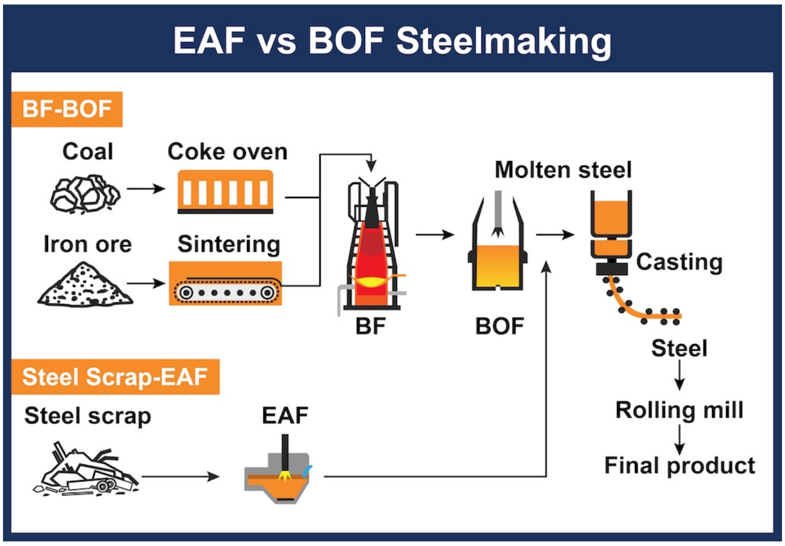

Figure 1.1: Comparison of EAF and BOF Processes [1]

In this thesis the focus is on the EAF method, but some findings on the impinging jet-bath interaction may also be relevant to the top-blowing used in the BOF method.

1.3 The Electric Arc Furnace

The Electric Arc Furnace has emerged as a more environmentally-friendly alternative to the BF-BOF method due to the large energy savings from bypassing the coke burning process, and by being able to repurpose old scrap steel instead of needing raw iron oxide. These important environmental benefits have enticed governments to pursue advancing this technology to develop a more sustainable future for steelmaking. [21]

1.3.1 The Stages of EAF Steelmaking

The EAF process, commonly referred to as the tap-to-tap cycle, is shown below and can be broken into 6 discrete steps [23]:

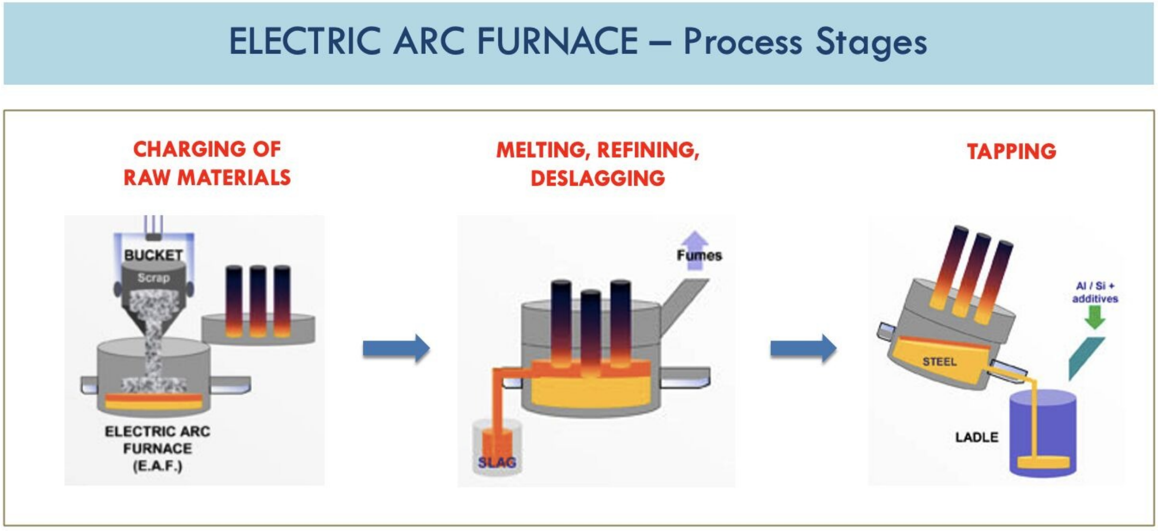

Figure 1.2: Different Stages of EAF Steelmaking [2]

1. Charging: The scrap steel and fluxes (such as Dolomite and Lime) are loaded into the furnace using a charge bucket, which is lowered into the furnace via an overhead crane.

2. Melting: Energy is added to the furnace using electric energy supplied via graphite electrodes which are placed into the scrap. To prevent the walls of the furnace from being damaged by the arcs, lower voltages are applied for the early melting phases. As the scrap is melted the voltage can be increased, and the electrodes can be raised to lengthen the electrical arcs, which increases the electrical power that is supplied to the melt, decreasing the time required to form the molten pool.

3. Refining: The chemical composition of the scrap steel is altered by removing contaminants such as phosphorus, sulfur, aluminum, silicon, manganese and carbon. It is also essential to keep dissolved gases such as hydrogen and nitrogen to acceptable levels. To remove these impurities oxygen is added to the bath which creates an oxidation reaction with the impurities in the bath forming oxides that float out of the steel and into the slag layer. This stage is extremely important as it directly shapes the final properties of the resulting steel through the decarburization reactions and removal of impurities.

4. De-Slagging: Impurities that are oxidized into the slag layer are removed from the furnace by tilting the furnace which pours the slag through the slag door. Removing the slag prevents the possibility of phosphorus reversion, which is where phosphorus can return from slag back into the molten bath during the tapping process.

5. Tapping: When the chemical composition and temperature in the bath reach the desired levels, the tap-hole in the furnace is opened, and the furnace is tilted which pours the molten steel into a ladle where it is then transferred for future refinement. During tapping bulk alloys are added to the steel based on bath measurements to reach desired steel qualities. For some steel grades, like stainless steel, slag is also added to the ladle. Before further processing de-oxidizers, such as aluminum or silicon, are introduced into the steel to lower the oxygen content.

6. Furnace Turn-Around: The slag door is cleaned of solidified slag, the walls, cooling components, and electrodes are examined for signs of damage and the taphole is filled with sand. Frequently a few tonnes of steel and slag are left in the furnace following the tapping process to speed up the melting process of the subsequent charge of scrap.

Overall the entire process typically takes a 90-tonne, medium power furnace around 60 minutes, with some double shell furnace operations being able to decrease the tap-to-tap time to roughly 30-40 minutes. [23]

1.4 Stirring in the Electric Arc Furnace

In the EAF process stirring the bath is incredibly important because the reactions in the bath are rate-limited by the amount of oxygen that can reach into the bath. Increasing the stirring in the bath allows for oxygen to penetrate faster and further into the bath increasing the rate of the decarburization reactions. This decreases the time needed to refine the molten steel, increasing efficiency and saving energy.

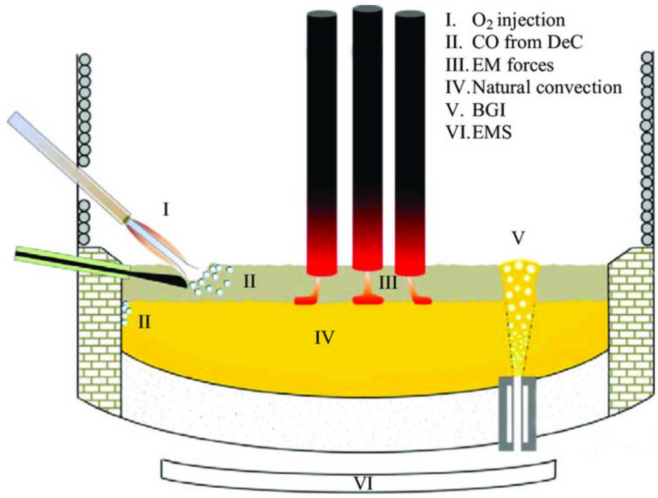

Figure 1.3: Different stirring forces that improve the motion of liquid steel in the bath during the EAF process [3]

There are six main mechanisms that can stir the bath in the EAF process. [3] These processes are shown in Figure 1.3.

1. O_2 Injection: Oxygen is accelerated from a jet onto the surface of the bath to transport oxygen to the surface of the bath to enhance reactions. The momentum from the oxygen is also imparted into the bath, which stirs it and creates a cavity at the impact point.

2. CO from DeC: The oxygen provided from the jet reacts with the carbon dissolved in the bath to create CO bubbles near the surface of the impact zone. The bubbles are pushed upwards through the bath due to buoyancy which stirs the bath.

3. EM Forces: The movement of free electrons through the molten steel creates a magnetic force that can stir the bath.

4. Natural Convection: The local differences of temperature and chemical composition create an imbalance in density in the bath. The differing densities create buoyant forces that drive a global circulation in the bath.

5. Bottom Gas Injection (BGI): A gas is injected through a plug at the bottom of the furnace, which then rises due to buoyant forces. The shear forces from the rising bubbles on the surrounding liquid create a strong mixing effect.

6. Electromagnetic Stirring (EMS): A magnetic field is created by passing a low-frequency AC current through coils located under the furnace. This generates a magnetic field that drives the molten steel, increasing mixing.

The main stirring methods that will be analyzed in this thesis are oxygen injection and the CO bubbles that are formed as a result of the oxygen injection.

1.4.1 Top-Blowing from a Supersonic Jet

To inject oxygen into the bath a lance is inserted into the furnace to blow the oxygen onto the surface of the metal bath. To increase the mixing in the bath, the oxygen is injected supersonically which allows it to impart more momentum into the bath on impact. To ensure that the maximum amount of momentum is transferred the lance is positioned such that the core of the supersonic jet reaches the surface of the bath. For a standard supersonic jet the core length is found to be between 15-35D, which requires the lance to be extremely close to the bath. However, in the bath the conditions are harsh, with high ambient temperatures and considerable splashing from the molten metal due to the imparted momentum from the jet. To mitigate this issue a coherent jet is used, which extends the reach of the potential core up to 70D, protecting the lance from the splashing metal. [4] [24]

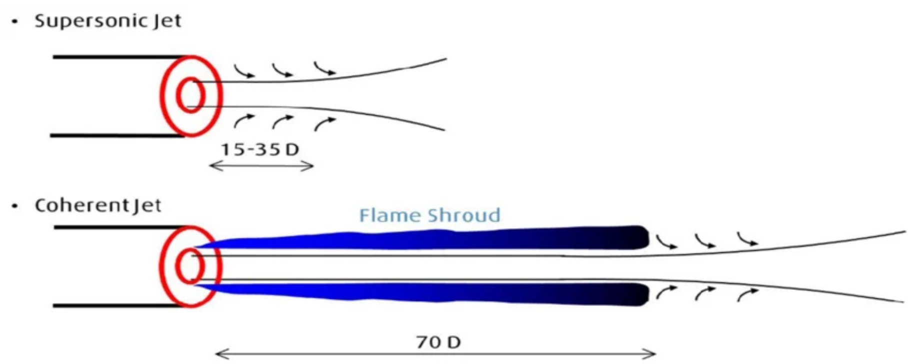

Figure 1.4: Comparison between standard supersonic jet and coherent jet [4]

Coherent Supersonic Jet

The coherent jet works by shielding the potential core of the jet from the shear layer by igniting a flame surrounding the potential core. This delays the turbulent mixing until the core has reached further downstream shown in Figure 1.5.a. [24]

To create the flame around the core the primary oxygen inlet is surrounded by annular rings of fuel inlets and secondary oxygen inlets. These subsonic inlets are placed such that the oxygen and fuel from these inlets form a stoichiometric mix that ignites to form a flame that surrounds the supersonic jet core. This layout for the lance inlets is shown in Figure 1.5.b.

The flame formed around the supersonic jet core limits the mixing between the jet core and the ambient air, extending the length of the potential core. This allows more momentum to reach the surface of the bath creating a larger cavity and increasing the mixing in the bath.

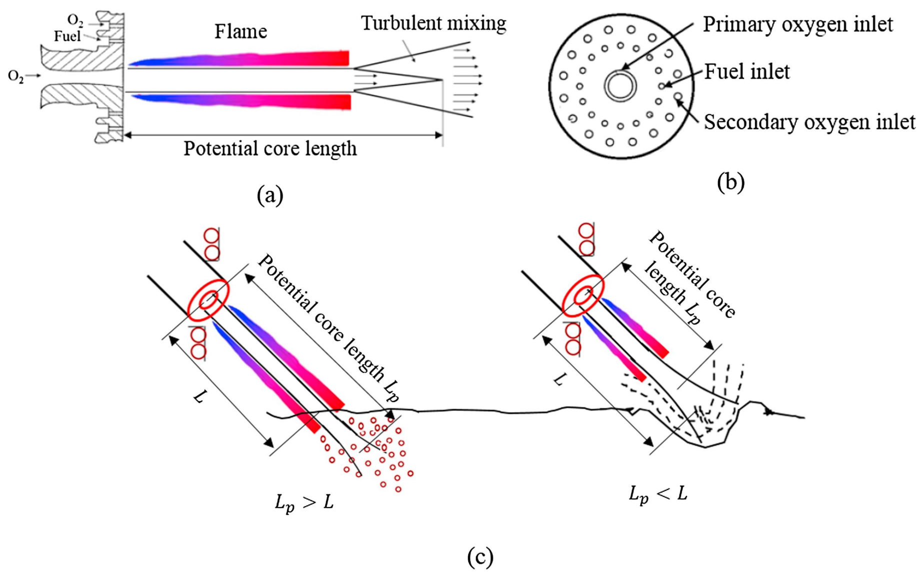

Figure 1.5: Coherent jet use in EAF [5]

Cavity Formation and Momentum Mixing

The momentum from the impinging jet creates a depression in the liquid. The gas travels radially outward from the impact point along the bath surface. This shear from the impinging air passing along the surface of the bath drives recirculation in the bath.

The shape of the cavity that is formed depends on the momentum of the gas jet that impacts the surface, and the properties of the liquid that comprises the bath. The momentum that impacts the surface of the bath depends on the distance that the potential core has to travel, and the velocity of the core flow leaving the lance. Thus properties of the cavity can be controlled by modulating the velocity of the core flow and the position of the lance with respect to the bath surface.

The cavities formed from the gas impingement can be classified into 3 distinct categories: [6]

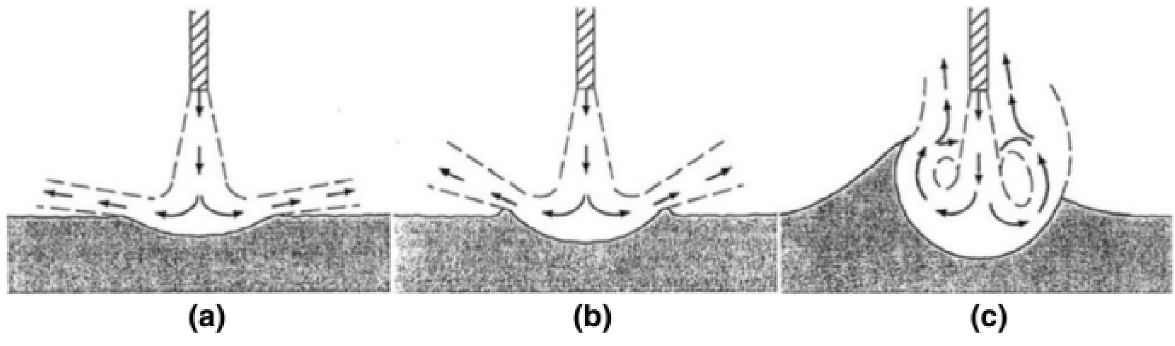

Figure 1.6: Different deformation modes for impinging gas jet on liquid surface. a) Dimpling, b) Splashing c) Penetrating [6]

1. Dimpling: Dimpling is observed when the jet momentum is low, or when the distance between the nozzle and the bath is high relative to the core length. The dimpling mode is characterized by only a slight depression in the surface of the liquid, and low energy transfer to the bulk fluid. Overall the low turbulent energy imparted on the liquid makes the dimpling mode largely insufficient at agitating the bath, and the cavity formed remains steady [25].

2. Splashing: As the jet momentum increases or the jet is moved closer to the liquid, the cavity mode transitions from dimpling to splashing. In the splashing mode, the depression becomes deeper and

wider, while the air flow exiting the cavity remains largely horizontal. However, the cavity becomes unsteady as ripples form periodically around the lip of the depression as the depth of the cavity begins to lightly oscillate.

3. Penetrating: Moving the nozzle closer to the surface, or further increasing the momentum of the jet transitions the depression from splashing to penetrating. This mode is characterized by a significant increase in the depth of the cavity, while the walls of the cavity transition to be nearly vertical. The lip, which marks the edge of the cavity, is elevated well above the original height of the bath. The ripples transition to waves and move more distinctly outwards from the center of the cavity, while the depth of the cavity oscillates much more significantly than in the splashing mode.

In this thesis the penetrating mode is the main mode that is studied due to its wide use in the steelmaking process as a result of its superior mixing properties compared to the other modes.

1.4.2 Mixing from Bubble Formation

Due to the elevated temperature in the furnace, and the high turbulent mixing at the surface of the bath, the oxygen from the impinging coherent jet creates two main reactions near the liquid-gas interface.

First, at the surface of the exposed liquid metal, a film of oxides, composed mostly of FeO, is formed due to the high local concentration of O_2. This reaction is exothermic, generating considerable heat that helps maintain the high temperature needed in the refining process. The oxides formed in this reaction make up the slag, which covers the surface of the liquid metal. [7]

Second, in carbon-containing baths, decarburization is the principal reaction that occurs near the surface of the depression formed from oxygen blowing. The decarburization is the reaction between the carbon dissolved throughout the bath, and the oxygen that is blown onto the bath. This reaction forms a Carbon Monoxide (CO) gas that takes the form of a bubble that can then be pushed under the surface of the cavity due to the high turbulence caused by the coherent jet interacting with the bath. [7]

These reactions are shown in Figure 1.7.

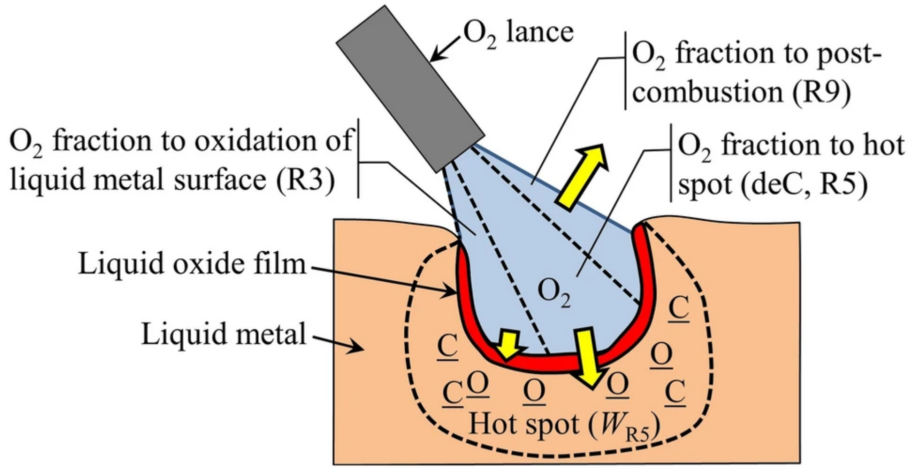

Figure 1.7: Mixture of species present at cavity interface [7]

The CO bubbles formed from the decarburization reaction are then subject to the bulk movement of the liquid caused by the momentum from the jet. This macroscale movement of bubbles is shown in Figure 1.8.

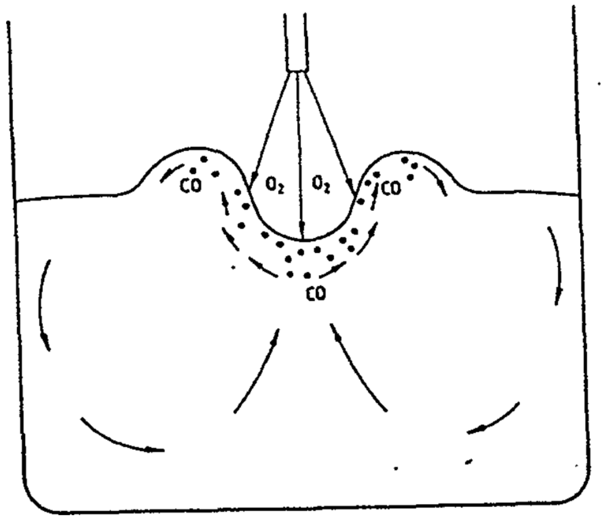

Figure 1.8: Bubble recirculation from an Impinging Jet [8]

In addition to this bulk movement, the bubbles are also subject to an immense buoyancy force due to the large difference in density between the CO bubble and the mostly iron bath. The buoyancy accelerates the bubble upwards relative to the bulk flow, and due to the difference in velocities between the bubble and the surrounding fluid, a drag force is also applied to the bubble. The drag force acting downwards on the bubble imposes an opposing upward force of equal magnitude on the bulk of the fluid, enhancing the velocity of the bath.

1.5 Objectives of the Thesis

The goal of the work conducted in this thesis is to improve current models regarding the jet-bath interaction in the EAF steelmaking process. The work comprising this thesis is composed of expanding the validation of current CFD models to be able to more accurately capture the physics of the interaction. The primary content areas of the research are:

1. To validate the accuracy of the VOF model in predicting momentum-based properties from top-blowing impinging gas jets.
2. To determine the impact of gas bubble entrainment on the properties of the cavity.
3. To expand the use of the VOF model to realistic furnace conditions, and compare the results with a simplified representative simulation.

Chapter 2

Jet-Bath Interaction

The desire to improve the EAF process and produce steel in a more sustainable manner requires the steelmaking process to be well understood. One underdeveloped subject of importance is the interaction between the supersonic coherent jet and the molten steel bath. This interaction is what determines the length of the refining stage of the steelmaking process. If the impact of different jet parameters on the mixing rate in the bath can be characterized, the refining process can be optimized to reduce the amount of time and energy required to produce steel. Thus, the end goal is to be able to model the mixing in the bath as a function of the jet parameters.

However, the jet-bath interaction is a complex problem with many different physics playing an important role in the process. Some important phenomena include the formation of the cavity, mixing induced by the momentum of the jet, slag formation, surface reactions, bubble formation, natural convection, among others. The deep complexity of this problem means that assumptions will have to be made in creating a model and the impact of these assumptions must be studied.

In this study the first step towards characterizing these complex physics is to verify that the tools used are able to accurately model them. This requires the use of simplified test cases that can isolate the different physics at work and compare the simulation results with those of experiments. This allows different physics to be gradually added to the model and the error for each of these additions can be characterized.

2.1 Top-Blowing Subsonic Impinging Air Jet on Water

The first simplified step towards studying the impinging jet in the EAF process is to study a vertical impinging jet of air onto a surface of water. This perpendicular subsonic impinging jet on a liquid surface was characterized in experiments conducted by Banks and Chandrasekhara. In this experiment they characterized the cavity depth, cavity width, and lip height as a function of the independent variables labeled in Figure 2.1. Transient physics of the cavity like cavity oscillation, ripple formation, and circulation were not investigated. [10]

To fully characterize the cavity, 282 experiments were conducted by varying the parameters shown in Table 2.1 to measure a wide range of cavity responses.

Nozzle Diameter (d_0)	0.25, 0.5, 0.75 in
Nozzle Width (b_0)	$\frac{1}{16}$ in
Nozzle Elevation (H)	0.1 to 1.0 ft
Water Depth (D)	0.83 to 3.0 ft
Nozzle Velocity (V_j)	25.2 to 420 ft/s
Volumetric Flow Rate (Q)	0.0086 to 1.158 ft^3/sec (STP)
Nozzle Reynolds Number (R_j)	2150 to 80,000

Table 2.1: Range of values used in the experiment

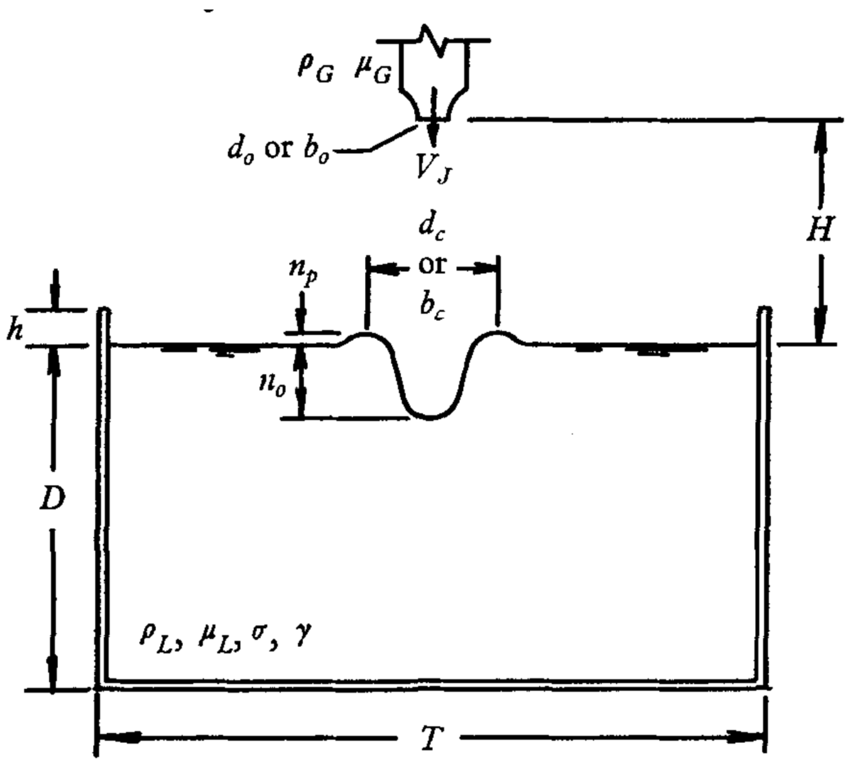

Figure 2.1: Description of experimental parameters

2.1.1 Cavity Depth

Banks and Chandrasekhara characterized the depth of the cavity by assuming that the weight of the liquid displaced in the cavity, was equal to the force exerted by the jet onto the liquid. After adding the surface tension of the liquid they obtained the expression:

$$\frac{n_0}{H} = \frac{(\frac{\pi}{B_*})^{\frac{1}{2}}}{(\frac{M}{\gamma L n_0^3})^{\frac{1}{2}} - (\frac{\pi}{B_*})^{\frac{1}{2}}} \tag{2.1}$$

where $B_* = 125$, n_0 is the depth of the cavity, H is the height of the nozzle, and γ is the density of the liquid.

The depth results of the experiment along with the analytical correlation calculated with Eq. 2.1 are shown in Figure 2.2.

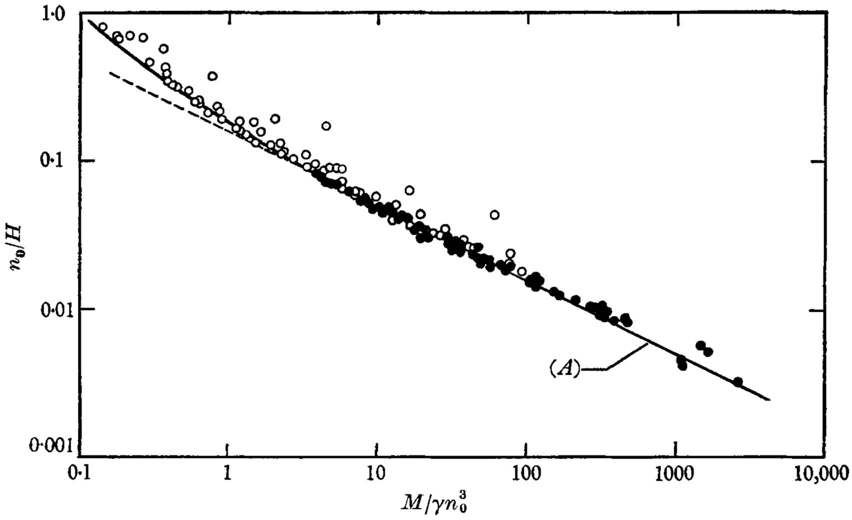

Figure 2.2: Non-dimensional depth data measured for the subsonic impinging round jet. ○: deep water tests, ●: shallow water tests

2.1.2 Cavity Shape

The cavity shape relation was further developed by Cheslak, Nicholls, and Sichel who used the equilibrium between the weight of the displaced liquid, and the static pressure from the jet while assuming that the cavity takes the shape of a paraboloid. [9]

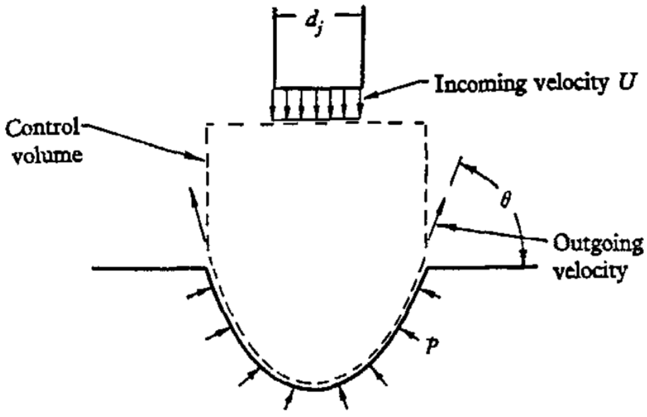

Figure 2.3: Assumed paraboloid shape used for correlation [9]

By assuming the reflecting jet leaving the cavity exits at angle θ, a force balance is calculated yielding the non-dimensional diameter as:

$$\zeta_3 = 2^{\frac{3}{2}}[\frac{M_3}{\pi} - 1 + (\frac{2M_3}{\pi} + 1)^{\frac{1}{2}}]^{\frac{1}{2}} \tag{2.2}$$

where M_3 is a non-dimensional axisymmetric momentum defined as:

$$M_3 = \frac{M}{\gamma_L a^3} \tag{2.3}$$

The calculated cavity diameter relation from Eq. 2.2 is then compared to experimental data collected by Banks and Chandrasekhara [10], and Cheslak [9] to verify the accuracy of the prediction.

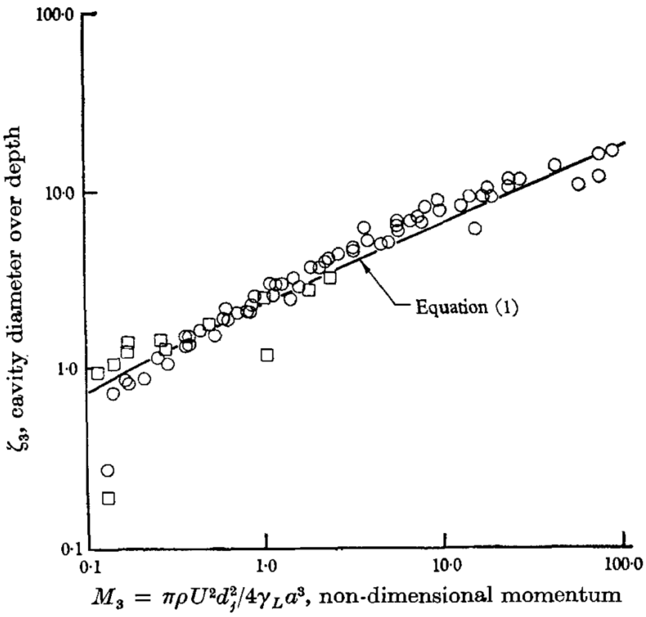

Figure 2.4: Plot of non-dimensional diameter (ζ) versus non-dimensional momentum (M_3), □: Experimental results from Cheslak [9], ○: Experimental results from Banks [10]

Analyzing Figure 2.4 shows good agreement for the theoretical prediction for the size, and shape of a cavity formed from a subsonic impinging jet. As camera technology improved, more sophisticated image processing was able to be used to directly measure the shape of the cavity. Experiments conducted by Evestedt and Medvedev found that the cavity mostly agreed with the parabolic assumption, but there were cases where the cavity was found to be more Gaussian, or elliptical. These cases were defined as deep cavities, which occur in the penetrating cavity regime. Comparing the results with the previous experiments showed that the previous methods overestimated the width and height of the cavity. The reasoning attributed to this inaccuracy is that the previous theories didn't account for the surface tension or viscosity of the liquid [26].

2.2 Expansion of Theory Towards EAF Conditions

To determine the validity of the correlations derived from experiments based on water models, it is imperative to analyze the impacts of the different simplifications that are made to use these models. In the EAF process there are many secondary effects that impact the cavity characteristics, like ambient temperature, the slag layer, and chemical reactions among others.

2.2.1 Impact of Differences in Ambient Temperature

To determine the impact of changing the ambient temperature of the domain on the jet, Sumi et al. [12] conducted an experiment in which the properties of a supersonic jet in different ambient temperatures were measured. A CFD study was then conducted by Alam et al. [11] comparing a k-ϵ model with the previously mentioned experimental results.

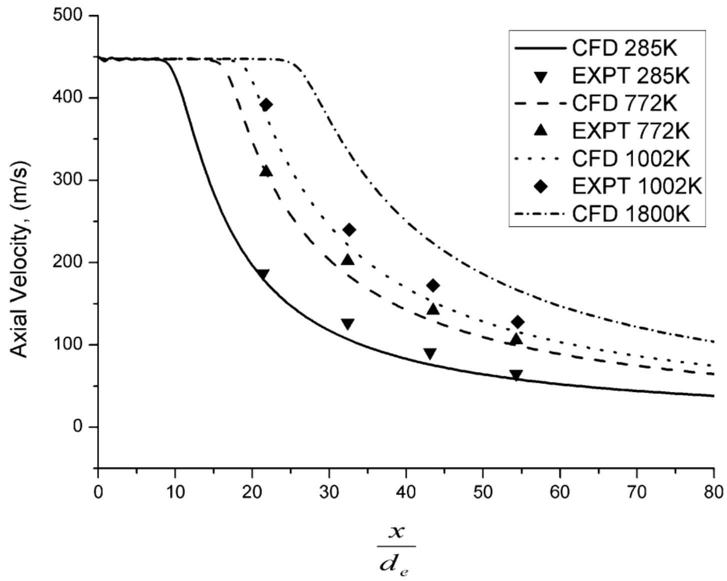

Figure 2.5: Velocity distribution on the center axis results for k-ϵ simulation [11] and experimental results [12].

The results from these studies show that the axial velocity from the jet is dependent on the temperature of the ambient air, especially regarding the length of the jet core. It was found that the jet velocity is constant, and independent of the ambient temperature in the jet core region.

From the results of the experiments, a relation for the axial centerline velocity of a cold jet in different ambient temperatures was developed by Ito and Muci [27].

The axial centerline velocity is expressed as:

$$\overline{u}_c(\overline{x}) = 1 - exp(\frac{-1}{2(\alpha\overline{x}\sqrt{\overline{\rho}_{out}} - \beta)}) \tag{2.4}$$

Where $\overline{\rho}_{out}$ is the non-dimensional density equal to ρ_{amb}/ρ_{out}, $\overline{x}$ is the axial distance non-dimensionalized by the nozzle diameter, and α and β are non-dimensional constants equal to 0.0841, and 0.06035 respectively. The non-dimensional potential core length is then calculated as:

$$\overline{x}_{core} = \frac{\beta}{\alpha\sqrt{\overline{\rho}_{out}}} \tag{2.5}$$

Equations 2.4 and 2.5 show that the difference in jet properties in different ambient temperatures can be explained by the density differences that arise as the temperature of the ambient gas is increased. This increase in velocity as a result of the temperature difference will create an error in the analysis of the cavity depth because the water model relations were calculated using the jet-spreading at an ambient room temperature. Thus, more momentum will reach the cavity in the higher temperature cases leading to an under-prediction in the cavity depth. It is important to notice that the jets at different temperatures are comparable in the potential core region as the velocities are constant with respect to temperature in this region.

2.2.2 Impact of the Slag Layer

In the real EAF process, a gas jet first impinges upon the slag layer exchanging mass, momentum, and heat. This directly reduces the impact of the jet with regard to cavity formation and mixing in the bath. Therefore it is important to analyze the impact of the addition of the slag layer in the multiphase interaction. However, it is difficult to directly collect measurements of the bath during the EAF process due to the high temperatures, the opaque nature of the steel and slag, and potential splashing that can damage measurement devices. Qian et al. [13] created a physical model of this interaction by using an air jet and water bath and introducing a thin pseudo-slag layer composed of kerosene and corn oil. The slag thickness was kept constant while the jet momentum and height were varied allowing for the collection of cavity depth data for different blowing conditions comparable to previous air-water studies. These results are shown in Figure 2.6.

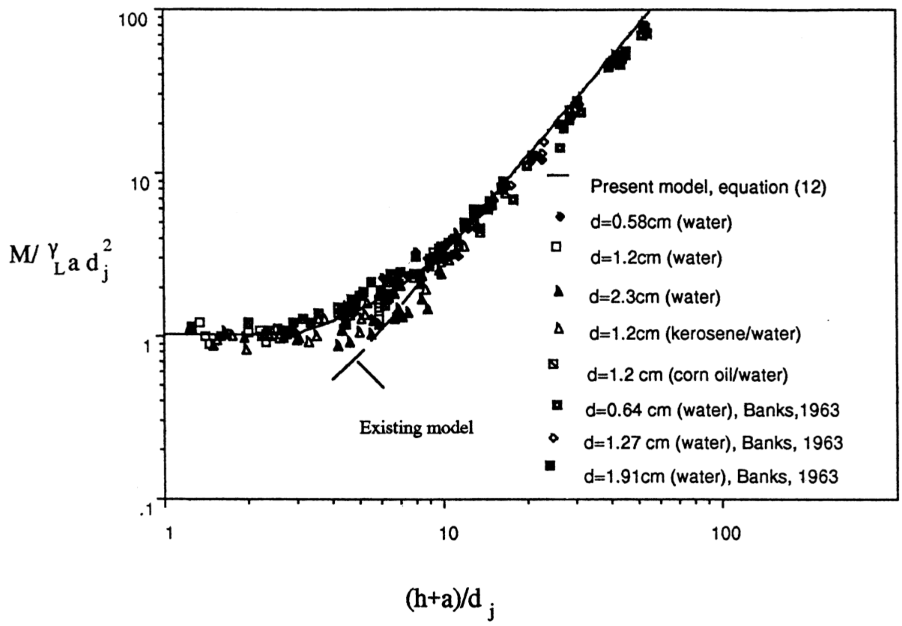

Figure 2.6: Nondimensional momentum vs. Nondimensional depth for different liquid compositions [13].

From the depth data collected, and using the energy balance principles from Banks and Chandrasekhara [10], and Cheslak et al. [9], a new relation was developed to describe the multi-liquid response. The model they derived is calculated as:

$$\frac{M}{\gamma_{Lmix} a d_j^2} = \frac{\pi}{2K_2^2}\left(\frac{h+a}{d_j}\right)^2 \tag{2.6}$$

where M is the jet momentum, a is the depth of the cavity, d_j is the diameter of the jet, K_2 is a constant chosen as 7.5, h is the height of the jet, and γ_{Lmix} is the weighted specific weight mixture of the two liquids defined as:

$$\gamma_{Lmix} = \frac{a_1}{a}\gamma_{L1} + max[\gamma_{L1}(1-\frac{a_1}{a}), \gamma_{L2}(1-\frac{a_1}{a})] \tag{2.7}$$

where a_1 is the thickness of the slag layer, γ_{L1} is the specific weight of the slag layer, γ_{L2} is the specific weight of the liquid comprising the bath.

Analyzing this relation with the experimental results, and the previous single-layer liquid model shows good agreement for both single-layer and two-layer cavity depths. If the slag layer is removed from this two-layer analysis the model returns to the previously derived single-layer depth correlation. This shows that the impact of the slag layer on the formation of the cavity can be accurately accounted for using this correlation.

2.2.3 Impact of Surface Chemical Reactions

To determine if the chemical reactions at the surface of the cavity have an impact on the cavity geometry Cheslak et al. [9] conducted an experiment measuring the cavity depth imposed by an impinging jet onto liquids of different materials. The non-dimensional cavity depth as a function of the liquid and jet parameters could then be calculated using the relations that were derived to describe the water model. The materials chosen for the liquid were mercury, cement, water, and molten iron. The cavity depth results for the reactive molten iron are then compared to the other liquids, and the theoretical model shown in Figure 2.7.

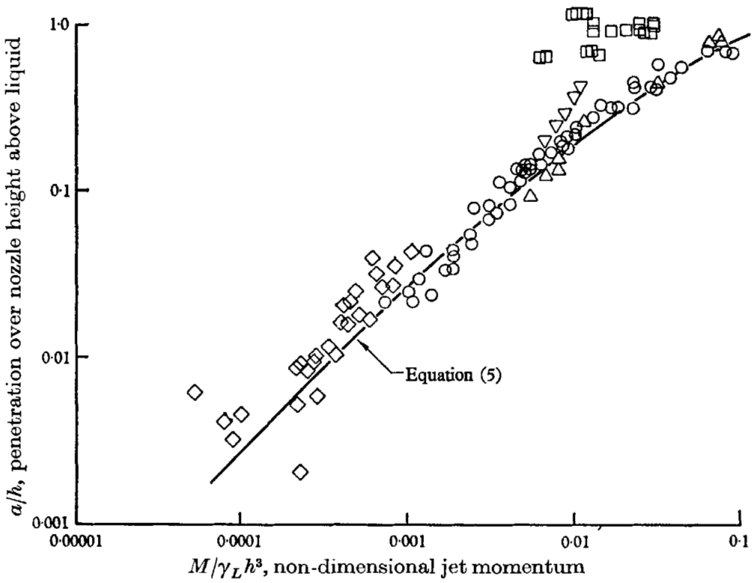

Figure 2.7: Plot of non-dimensional depth versus non-dimensional jet momentum for different liquids.◇, Water; ∇, Mercury; ○, cement; △, water; □, molten iron [9]

Analysis of the results reveals that the depth of the cavity in the molten iron case is noticeably under-predicted by the theoretical analysis. This result was attributed to the chemical reactions at the surface as the other inert materials with varying densities are represented well by the theoretical prediction. A theoretical model for the impact of chemical reactions was not derived so predicting the effect of excluding this phenomenon in the simulation isn't possible. Therefore it would be of interest to try to emulate these physics and their impact on the bath.

2.2.4 Impact of Replacing the Coherent Jet with a Standard Supersonic Jet

In the previous studies that characterized the size and shape of the cavity, a standard cold jet was used. This differs greatly from the EAF process which uses a shrouded coherent jet to extend the potential core region of the jet onto the surface of the bath. This extension of the potential core region causes the cavity response to diverge from the water models due to the additional jet momentum reaching the surface, much like for the cases with an elevated ambient temperature.

To describe and characterize the differences in the cavity response between the different jets, Wei et al. [28] conducted a CFD simulation using the $k-\epsilon$, and VOF models. The simulations used the different jets impinging onto a surface of molten steel with an ambient temperature of 1600 °C. The simulation also included a slag layer with the same thickness for both simulations. The physical properties of the different fluids are shown in Table 2.2.

Material	Viscosity ($kgm^{-1}s^{-1}$)	Density (kgm^{-3})	Surface Tension (Nm^{-1})
Steel	0.0065	7200	1.6
Slag	.35	3000	1.2

Table 2.2: Physical properties of the fluids

To be able to accurately model the impact the different jets have on the cavity, the momentum of the jets vs. the axial distance from the jet nozzle must be analyzed. To do this the centerline velocity of the jets was measured to compare the effective potential core lengths. The centerline velocity for the different jets is shown in Figure 2.8.

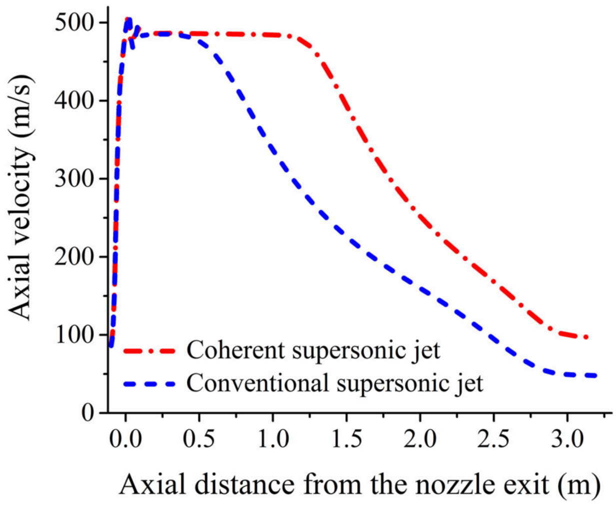

Figure 2.8: Axial velocity distributions for the coherent and conventional supersonic jets

The results show that the coherent supersonic jet behaves similarly to the case of the cold jet in a hot atmosphere. The potential core length is extended much further than for the conventional supersonic jet, while the potential core velocity is the same for both cases. Next the impact of the different jets on the bath surface is studied inside, and beyond the potential core region.

To produce a model of the penetration depth, the previous air-water and air-water-oil derived models were used to arrive at:

$$h_p = \sigma \frac{\rho_c^2 \rho_e \rho_x v_e D_e}{(\rho_{steel}^2 g)^{\cdot} 5} \left(\frac{k}{H_o - h_g}\right)^{\frac{1}{2}} + \frac{\rho_{steel} - \rho_{slag}}{\rho_{steel}} h_g \tag{2.8}$$

where ρ_e is jet exit density, ρ_x is the jet density at the bath surface, v_e is the jet exit velocity, D_e is the jet diameter, H_o is the lance height, h_g is the slag thickness, g is the gravitational constant, and k is a nondimensional parameter reflecting jet attenuation defined as:

$$\left(\frac{v_x}{v_e}\right)\left(\frac{H}{D_e}\right) \tag{2.9}$$

and ρ_c is a density-based parameter to study which model is best able to capture the effect of the slag layer, with the values calculated as:

$$\rho_C = \begin{cases} \rho_{steel} & \text{Theoretical model} \\ \dfrac{\rho_{steel} + \rho_{slag}}{2} & \text{Modified model 1} \\ \rho_{slag} & \text{Modified model 2} \end{cases} \tag{2.10}$$

The depth results for the different jets for different lance heights are shown in Figure 2.9.

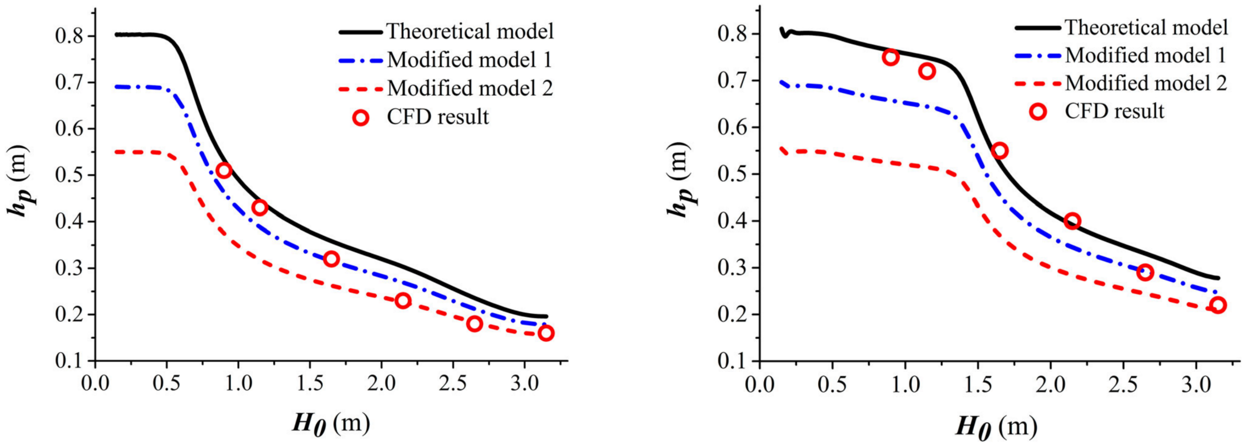

(a) Jet penetration results for standard supersonic jet (b) Jet penetration results for coherent supersonic jet

Figure 2.9: Comparison of standard and coherent supersonic jet penetration depths

The results from the CFD simulations show that the cavity depth trends follow the trends found in the potential core velocity. There is a set of lance heights below which the cavity depth remains nearly constant due to the jet potential core being able to penetrate into the bath. Above these heights the measured depth gradually decreases as the momentum of the jet disperses.

One important quality to note is that for both the standard and coherent jets the maximum depth is roughly the same when the potential core reaches the bath. This, in theory, would allow for the direct comparison of cavities formed from standard supersonic jets, and coherent supersonic jets as long as the lance height is carefully selected to remain below the potential core length for both jets.

2.3 Cavities Formed From Angled Jets

In the EAF process the jets blowing oxygen onto the surface of the bath aren't strictly vertical. Instead, the jet is often angled to give the jet velocity a lateral component, enlarging the impact area and promoting circulation instead of only forming a deep vertical cavity. This enhanced surface area and bath velocity increases the chemical reaction rate, which reduces the mixing time in the bath, saving energy.

The cavity formed as the result of an impinging jet at an angle was first analyzed by Collins and Lubinska [29]. In this experiment they varied the angle of an air jet impinging onto a water surface. The penetration of the jet was expressed as a function of the thrust from the jet (τ), the angle of penetration (θ), and the specific weight of the liquid ω shown in Eq 2.11.

$$P = \frac{53\tau sin\theta}{x^2\omega + 19(\omega\tau^2)^{\frac{1}{3}}} \tag{2.11}$$

This correlation was expanded upon by Alam et al. [14], who analyzed the problem through the stagnation pressure analysis method introduced by Banks and Chandrasekhara [10]. A schematic of the problem they considered is shown in Figure 2.10. The depth of the cavity (P) was derived to be a function of the jet momentum M, the diagonal height of the jet H, the angle of the jet θ and a fitted multiplicative constant K_2, shown in Eq. 2.12.

$$\frac{Mcos\theta}{\rho_l g H^3} = \frac{\pi}{2K_2^2}(\frac{P}{H})(\frac{P}{Hcos\theta} + 1)^2 \tag{2.12}$$

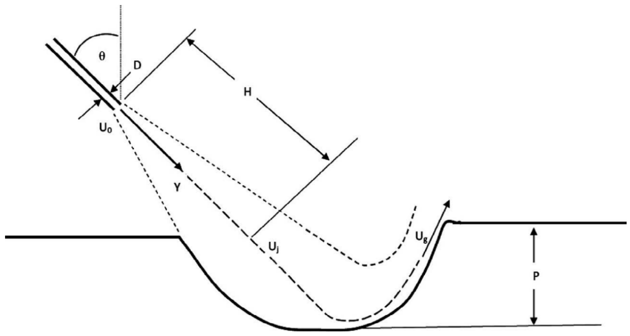

Figure 2.10: Schematic of inclined jetting [14]

The theoretical model was then verified by conducting an experiment using a gas jet impinging on a surface of water at an angle. The angles chosen for the lance were 35°, 40°, 45°, with the distance of the jet from the liquid surface ranging from 65-165 mm, and flow rates of 0.43, 0.57, 0.71 Nm^3/min for a lance diameter of 14 mm. The depth results from the experiment are then compared with the theoretical formula, which is plotted in Figure 2.11. The slope of the line from the equation is the variable K_2, which was fitted to the experimental data, and found to be 7.4. This is in the range of other values found for K_2 (6.4 to 7.9), which were found by other researchers. [10] [30] [31] [13]

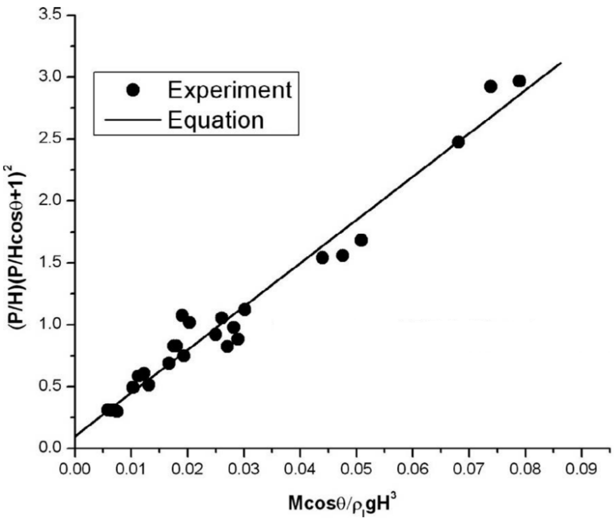

Figure 2.11: Cavity depth vs. dimensionless jet momentum for correlation and experimental results [14]

2.4 Oscillation of the Cavity Surface

Cavity Oscillation from a Perpendicular Jet

The onset of an oscillatory cavity response for higher jet momentum cases has been well described in the literature [10] [6]. The different oscillation behaviors of the cavity can be cleanly separated into Molloy's 3 cavity modes [6]. In the dimpling regime, only a small indentation exists and disturbances on the surface are small. If the jet momentum is increased, or jet height reduced, the cavity enters the splashing phase where ripples form on the surface of the cavity causing the cavity to oscillate and splash. If the jet momentum is further increased, or jet height further decreased, the cavity enters the penetrating phase where the ripples formed on the surface of the cavity cause strong oscillations as they travel along the surface.

To analyze the frequency of the oscillating behavior found in these cavities Adib et al. compared the

FFTs of the cavity response obtained from an experiment, and from a CFD simulation. They found a close match between the first 2 FFT modes, with the first experimental modes being 9, 11 Hz, and the first simulation modes being 9, 10 Hz. [32] This is in agreement with the range in frequencies found in other studies, 4 to 12 Hz.

However, there is a lack of literature that characterizes the amplitude and frequency of the oscillations as a function of the jet parameters. There is uncertainty in the direct relationship between oscillatory behavior and lance height found in the literature. Lee et al. [33] found a strong linear relationship between the two, while Lee et al. [15] reported that the oscillatory waves are independent of jet height and angle.

Cavity Oscillation from an Angled Jet

In the case of the angled jet, after the jet reaches the cavity, the cavity deforms to its maximum depth. After reaching this maximum, the cavity moves upwards and outwards away from the jet. This forms an elevated ridge in the cavity, called the knuckle. As the cavity is translated outwards by the momentum from the jet, another cavity begins to form in its place repeating the cycle. [15] A schematic showing the geometry of the cavities, and the knuckle separating them is shown in Figure 2.12.

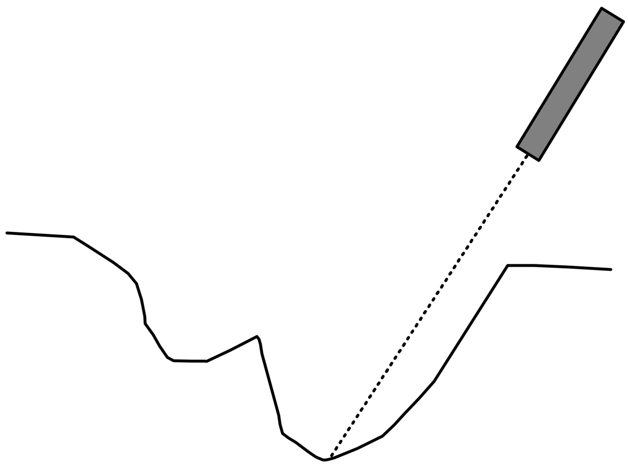

Figure 2.12: Schematic of angled cavity oscillation motion [15]

In the angled jet case, the oscillating behavior of the cavity directly changes the shape of the cavity, which makes it difficult to measure the size and frequencies of the oscillations. There have been no correlations developed to characterize the oscillatory behavior of the cavity formed by an angled jet.

2.5 Mixing Induced by the Top-Blowing Jet

To develop relations to characterize mixing behavior in the bath, the velocity in the bath must first be measured to provide a baseline to compare models to. Results from simulations and models can then be compared to the distribution of velocity found in the experiment. To measure the velocity in the bath Particle-Image-Velocimetry (PIV) is used. The PIV method works by using a camera to track particles that are injected into the flow. However, it has been shown that the PIV measurements of the particles are extremely sensitive to the quality of the images captured, which requires that the liquid-gas interface is accurately detected by the camera. To accurately measure the velocity profile in the bath Berger et al. [16] conducted an experiment to treat the PIV data and localize the moving interface.

To mitigate the issues of analyzing a chaotic 3D-flow field, a 2D planar jet was used. This allows the average flow-field to be accurately measured, and projected onto a 2D-plane. The geometry of the set-up used in the experiment is shown in Figure 2.13.

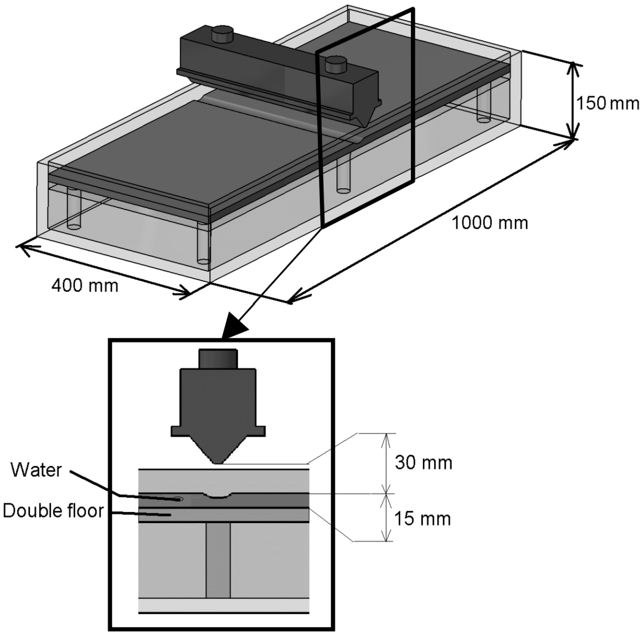

Figure 2.13: Schematic of 2D-impinging jet setup

The planar jet has a width of 5 mm, and the flow field is analyzed for Reynolds numbers of Re = 2000, 2700, which correspond to the dimpling and splashing regimes described by Molloy [6]. Using these low deformation modes allows the cavity to remain more stable which allows the resulting flow field to be more temporally stable.

From the treated PIV data, the cavity was able to be accurately placed in the dimpling and splashing conditions, which allowed for the separate analysis of the gas and liquid velocities around the cavity. The velocity fields for both phases, for both blowing conditions is given in Figure 2.14.

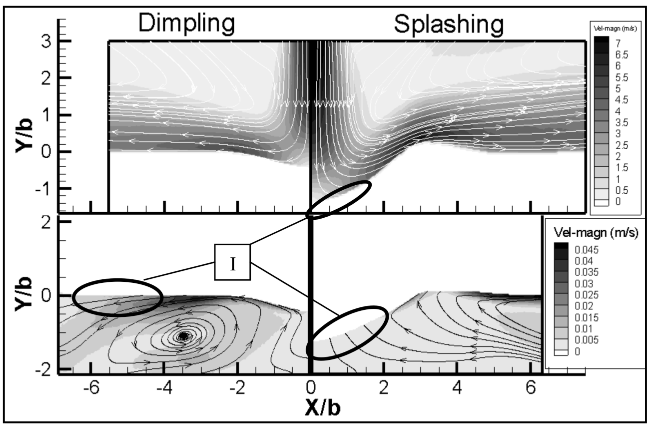

Figure 2.14: Water and air sides averaged velocity magnitude fields and streamlines X/b > 0: splashing configuration X/b < 0: dimpling configuration.

From the treated PIV data the shape of the cavity can then be analyzed from the accurate placement of the interface. The cavity measurements for the different cases are shown in Figure 2.15.

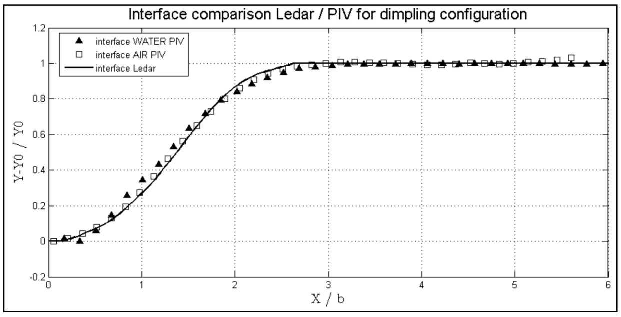

(a) Dimpling cavity shape

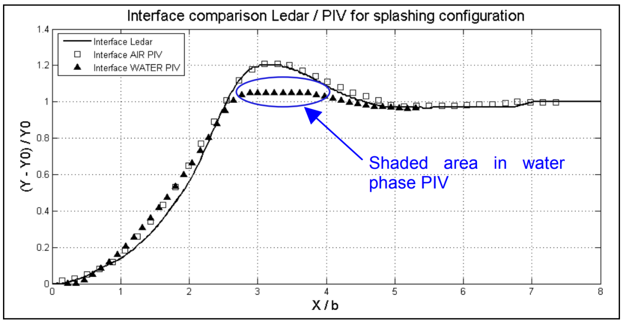

(b) Splashing cavity shape

Figure 2.15: Cavity shapes for the two different cavity modes [16]

The accuracy of the image processing algorithm, and spatial resolution of the cavity results in an uncertainty of ± 70 μm. This small margin of error makes this test case a good benchmark to test the VOF method. This case allows the model validation results to be compared to results with high fidelity, allowing more nuance in the comparison of the results.

Chapter 3

Numerical Environment

The aim of this section is to describe the physical laws that govern the physics, and the approximative methods used to solve them. The models used in this section are implemented using Simcenter STAR-CCM+, which is a commercial CFD and multiphysics software suite. STAR-CCM+ is widely used across many different fields including aerospace, automotive, and energy to simulate fluid flow, heat transfer, and stress interactions over a wide range of operating conditions. The software's capability to handle a wide range of physics phenomena makes it a good choice to use in the case of modeling the complex multiphysics in the EAF process.

In this section first the Navier-Stokes equations are defined which analytically describe the motion of fluids. Next, the solvers used to solve the fluid flow, and multiphase interaction are defined along with the spatial and temporal discretization of the fields. Finally the stagnation inlet boundary condition used to simulate the lance injection conditions is introduced.

3.1 Navier Stokes

The Navier-Stokes equations (NSE) describe the motion of viscous fluids using the conservation of mass, momentum, and energy shown in Equations 3.1, 3.2, and 3.3 respectively.

$$\frac{\partial \rho}{\partial t} + \vec{\nabla} \cdot (\rho \vec{u}) = 0 \tag{3.1}$$

$$\frac{\partial (\rho \vec{u})}{\partial t} + \vec{\nabla} \cdot (\rho \vec{u} \otimes \vec{u}) = -\vec{\nabla} p + \vec{\nabla} \cdot \overline{\overline{T}} + \vec{f} \tag{3.2}$$

$$\frac{\partial (\rho e)}{\partial t} + \vec{\nabla} \cdot (\rho e + p)\vec{u} = \vec{\nabla} \cdot (\overline{\overline{T}} \cdot \vec{u}) + \rho \vec{f} \vec{u} + \vec{\nabla} \cdot \vec{q} + r \tag{3.3}$$

where ρ is the density of the fluid, $\vec{u}$ is the velocity vector, p is the pressure, $\overline{\overline{T}}$ is the viscous shear stress tensor, $\vec{f}$ is the body force vector, e is the total energy, $\vec{q}$ is the heat flux variation, and r is the heat source term.

However, due to the large Reynolds numbers involved in the EAF process (1.5E6), the Navier-Stokes equations must be simplified to reduce the computational requirements. This is done by decomposing the Navier-Stokes equations into the Reynolds-Averaged Navier-Stokes equations (RANS).

3.2 RANS Model

To solve the Navier-Stokes equation the instantaneous flow properties are decomposed into a mean value, and the fluctuation around the mean, which when combined yield the original flow property.

$$\phi = \overline{\phi} + \phi' \tag{3.4}$$

When dealing with compressible flows, there is a nonlinearity that appears when trying to decompose the terms that depend on density and velocity because the density can no longer be considered constant. To solve this the quantity must be Favre averaged:

$$\phi = \tilde{\phi} + \phi" \\ \tilde{\phi} = \frac{\overline{\rho\phi}}{\overline{\rho}} \tag{3.5}$$

This allows for the mean mass, momentum, and energy transport equations to be written as:

$$\frac{\partial \rho}{\partial t} + \nabla \cdot (\rho \overline{\vec{u}}) = 0 \tag{3.6}$$

$$\frac{\partial}{\partial t}(\rho \overline{\vec{u}}) + \nabla \cdot (\rho \overline{\vec{u}} \otimes \overline{\vec{u}}) = -\nabla \cdot (\overline{p} + \frac{2}{3}\rho k) + \dot{\nabla}(\overline{T} + T_{RANS}) + f_b \tag{3.7}$$

$$\frac{\partial}{\partial t}(\rho \overline{e}) + \nabla \cdot (\rho \overline{e} \overline{\vec{u}}) = -\nabla \cdot (\overline{p} + \frac{2}{3}\rho k)\overline{\vec{u}} + \nabla \cdot (\overline{T} + T_{RANS})\overline{\vec{u}} - \nabla \cdot \overline{\vec{q}} + f_b \overline{\vec{u}} \tag{3.8}$$

Where the mean viscous stress tensor ($\overline{T}$) is defined as:

$$\overline{T} = \mu[\nabla \overline{\vec{u}} + (\nabla \overline{\vec{u}})^T] - \frac{2}{3}\mu(\nabla \cdot \overline{\vec{u}})I \tag{3.9}$$

, and the RANS stress (T_{RANS}) is defined as:

$$T_{RANS} = -\rho \overline{u_i' u_j'} + \frac{2}{3}\rho k I \tag{3.10}$$

The RANS stress tensor must then be modeled in terms of the mean flow quantities to provide closure to the mean mass, momentum, and energy equations.

To close the RANS equation, the SST-k-ω model was implemented. This model uses the Boussinesq approximation, assuming that the Reynolds stresses are proportional to the mean rates of deformation

$$-\rho \overline{u_i' u_j'} = \mu_t (\frac{\partial U_i}{\partial x_j} + \frac{\partial U_j}{\partial x_i}) - \frac{2}{3}(\rho k + \mu_t \frac{\partial U_k}{\partial x_k})\delta_{ij} \tag{3.11}$$

Where μ_t is the turbulent eddy viscosity, k is the turbulent kinetic energy, and δ_{ij} is the Kronecker delta.

The turbulent eddy viscosity in the SST-k-ω model is calculated as:

$$\mu_t = \rho k T \tag{3.12}$$

where T is the turbulent time scale that is calculated using Durbin's realizability constraint, which is defined as:

$$T = min(\frac{1}{max(\omega/\alpha*, (SF_2)/a_1)}, \frac{C_T}{\sqrt{3}S}) \tag{3.13}$$

$\alpha*$, a_1, and C_T are model coefficients that are defined in Table 3.1, while F_2 is a blending function calculated as:

$$F_2 = tanh((max(\frac{2\sqrt{k}}{\beta^* \omega d}, \frac{500\nu}{d^2\omega}))^2) \tag{3.14}$$

where β^* is a model coefficient, ν is the kinematic viscosity, and d is the distance from the cell to the wall.

In this model the turbulent kinetic energy k (m^2/s^2) and the specific dissipation rate ω (s^{-1}) are obtained from the following transport equations:

$$\frac{\partial}{\partial t}(\rho k) + \nabla \cdot (\rho k \overline{v}) = \nabla \cdot [(\mu + \sigma_k \mu_t)\nabla k] + P_k - \rho \beta^* f_{B^*}(\omega_k - w_0 k_0) + S_k \tag{3.15}$$

$$\frac{\partial}{\partial t}(\rho \omega) + \nabla \cdot (\rho \omega \overline{v}) = \nabla \cdot [(\mu + \sigma_\omega \mu_t)\nabla \omega] + P_\omega - \rho \beta f_B(\omega^2 - w_0^2) + S_\omega \tag{3.16}$$

Where P_k is the production of the turbulent kinetic energy defined as,

$$P_k = \mu_t f_c S^2 - \frac{2}{3}\rho k \nabla \cdot \overline{v} - \frac{2}{3}\mu_t (\nabla \cdot \overline{v})^2 + \nabla \overline{v} \tag{3.17}$$

and P_ω is the dissipation production defined as:

$$P_\omega = \rho \gamma [(S^2 - \frac{2}{3}(\nabla \cdot \overline{v})^2) - \frac{2}{3}\omega \nabla \cdot \overline{v}] + 2\rho(1 - F_1)\sigma_{\omega 2}\frac{1}{\omega}\nabla k \cdot \nabla \omega \tag{3.18}$$

Where F_1 is the blending function that combines the near-wall contribution of a coefficient to its value far away from the wall, which is calculated as:

$$F_1 = tanh([min(max(\frac{\sqrt{k}}{0.09\omega d}, \frac{500\nu}{d^2\omega}), \frac{2k}{d^2 CD_{kw}})]^4) \tag{3.19}$$

The coefficients used in these equations are given in Table 3.1.

a_1	0.31
α^*	1
β	$F_1\beta_1 + (1 - F_1)\beta_2$
β_1	0.075
β_2	0.0828
β^*	0.09
γ	$F_1\gamma_1 + (1 - F_1)\gamma_2$
γ_1	$\frac{\beta_1}{\beta^*} - \sigma_{\omega_1}\frac{\kappa^2}{\sqrt{\beta^*}}$
γ_2	$\frac{\beta_2}{\beta^*} - \sigma_{\omega_2}\frac{\kappa^2}{\sqrt{\beta^*}}$
κ	0.41
σ_k	$F_1\sigma_{k_1} + (1 - F_1)\sigma_{k_2}$
σ_{k1}	0.85
σ_{k2}	1
σ_ω	$F_1\sigma_{\omega_1} + (1 - F_1)\sigma_{\omega_2}$
$\sigma_{\omega 1}$	0.5
$\sigma_{\omega 2}$	0.856
C_T	0.6
$\lambda_2\frac{\beta}{\beta^*\alpha}$	0.075

Table 3.1: List of $k - \omega$ SST Parameters used.

3.3 Volume of Fluid Method

To capture the multiphase interaction between the impinging jet and the bath, the Volume of Fluid (VOF) model is used. The VOF model is a simple multiphase model that is suited to solving flows of multiple immiscible fluids. The VOF method is numerically efficient, and is best suited for simulations of flows where the different phases form larger structures, with relatively small contact areas between the different phases.

The distribution of the different phases is defined in terms of a variable called the volume fraction, which is defined as:

$$\alpha_i = \frac{V_i}{V} \tag{3.20}$$

where V_i is the volume of phase i in the cell, and V is the total volume of the mesh cell. Thus the volume fractions of all phases must sum to one:

$$\sum_{i=1}^{N} \alpha_i = 1 \tag{3.21}$$

where N is the number of phases.

The material properties of cells that contain a mixture of fluids can then be calculated using the volume fraction, and the properties of the individual fluid as:

$$\rho = \sum_{i}^{N} \rho_i \alpha_i \tag{3.22}$$

$$\mu = \sum_{i}^{N} \mu_i \alpha_i \tag{3.23}$$

$$C_p = \sum_{i}^{N} \frac{(C_P)_i \rho_i}{\rho} \alpha_i \tag{3.24}$$

where ρ_i is the density, μ_i is the dynamic viscosity, and $(C_p)_i$ is the specific heat of phase i.

The distribution of each phase is driven by the phase mass conservation equation:

$$\frac{\partial}{\partial t} \int_V \alpha_i dV + \oint_A \alpha_i v \cdot da = \int_V (S_{\alpha_i} - \frac{\alpha_i}{\rho_i} \frac{D\rho_i}{Dt} dV - \int_V \frac{1}{\rho_i} \nabla \cdot (\alpha_i \rho_i v_{d,i}) dV \tag{3.25}$$

where a is the surface area vector, v is the mass averaged velocity in the cell, $v_{d,i}$ is the diffusion velocity, S_{α_i} is a user-defined source term and $D\rho_i/Dt$ is the material or Lagrangian derivative of the phase densities.

To calculate the volume fractions of a two-phase flow the volume fraction transport is solved for only the first phase. Then the volume fraction of the second phase is adapted such that the sum of the volume fractions of the two phases is equal to one.

If more phases are introduced, the volume fraction equation is solved for every phase. Then the volume fraction for each phase is normalized by the total sum of the volume fractions in the cell.

Using the phase mass conservation, the multiphase interaction can be computed using adapted total mass, momentum and energy equations.

The total mass conservation for all phases is calculated as:

$$\frac{\partial}{\partial t}(\int_V \rho dV) + \oint_A \rho v \cdot da = \int_V S dV \tag{3.26}$$

where S is a mass source term related to the phase source term:

$$S = \sum_{i}^{N} S_{\alpha_i} \cdot \rho_i \tag{3.27}$$

The momentum equation for all phases is given by:

$$\frac{\partial}{\partial t}(\int_V \rho v dV)+\oint_A \rho v\otimes v\cdot da = -\oint_A pI\cdot da+\oint_A T\cdot da+\int_V \rho g dV+\int_V f_b dV-\sum_i^N \int_A \alpha_i\rho_i v_{d,i}\otimes v_{d,i}\cdot da+\int_V S_i^\alpha dV \tag{3.28}$$

where p is the pressure, I is the unity tensor, T is the stress tensor, f_b is the body forces vector, S_i^α is the phase momentum source term.

The energy equation is defined as:

$$\frac{\partial}{\partial t}\int_V \rho E dV + \oint_A [\rho H v + \sum_i^N \alpha_i\rho_i H_i v_{d,i}]\cdot da = -\oint_A \dot{q}" \cdot da + \oint_A T\cdot v da + \int_V f_b\cdot v dV + \int_V S_E dV \tag{3.29}$$

where E is the total energy, H is the total enthalpy, $\dot{q}"$ is the heat flux vector, and S_E is a user-defined energy source term.

The immiscibility of fluids is a result of the cohesion forces between their molecules, and depends on the properties of the fluid. The surface tension coefficient σ expresses the force per unit length acting along the interface between two fluids. Surface tension is a tensile force that acts tangentially to the interface between the fluids. The surface tension acts against outside forces to keep the fluid molecules at the surface attached to the rest of the fluid. It is imperative that this force is taken into account to more accurately model the shape and size of the cavity that results from the impinging jet.

The interfacial surface force is modeled as a volumetric force, which is resolved into two components:

$$f_\sigma = f_{\sigma,n} + f_{\sigma,t} \tag{3.30}$$

where:

$$f_{\sigma,n} = \sigma\kappa n \tag{3.31}$$

and:

$$f_{\sigma,t} = \frac{\partial\sigma}{\partial t}t \tag{3.32}$$

where σ is the experimentally calculated surface tension coefficient, n is the unit vector normal to the free surface, t is the tangential unit vector, κ is the mean curvature of the free surface.

The normal vector can be calculated using the volume fraction as:

$$n = \nabla\alpha_i \tag{3.33}$$

and is defined positive when pointing from liquid to gas. The curvature of the interface between the different fluids can then be expressed as:

$$\kappa = -\nabla\cdot\frac{\nabla\alpha_i}{|\nabla\alpha_i|} \tag{3.34}$$

The normal component of the surface tension force can then be calculated as:

$$f_{\sigma,n} = -\sigma\nabla\cdot(\frac{\nabla\alpha_i}{|\nabla\alpha_i|})\nabla\alpha_i \tag{3.35}$$

When the surface tension coefficient varies along the surface, which can be caused by temperature differences, the Marangoni or Benard convection can have a component that is tangent to the surface. This non-zero tangential force is evaluated as:

$$f_{\sigma,t} = (\nabla\sigma)_t|\nabla\alpha_i| \tag{3.36}$$

where, $(\nabla\sigma)_t$ is the tangential gradient of the surface tension coefficient.

3.4 Segregated Pressure Solver

In STAR-CCM+, the VOF method requires the use of a segregated flow solver to solve for the sharp interface, and large density differences between the cells. In a segregated solve the conservation of mass, and momentum are solved sequentially to get the solution variables. The solver uses a pressure-velocity coupling equation to fulfill mass conservation in the mesh. This coupling equation is derived from the continuity equation, and momentum equations to predict a velocity field that is consistent with the continuity requirement. In this work the SIMPLEC algorithm is used as the corrector, which assumes that the velocity corrections in the adjacent cells are equivalent to the corrections at the central cell such that:

$$v_p^{n+1} = v_p^* - \frac{V \nabla p'}{a_p^v + \sum_n a_n^v} \tag{3.37}$$

where a_n^v are the velocity neighbor coefficients, p' is the pressure correction, V is the cell volume, and v* is the intermediate velocity field from the discretized momentum.

The requirement of the segregated solver can become an issue due to the high coupling of pressure with other flow properties like density, temperature, and energy. The segregated solving of the conservation equations in this regime can lead to oscillations in the solution, divergence, slow convergence, and smearing of shocks.

3.5 Finite Volume Discretization

In transforming the model into a system of algebraic equations using the finite volume method (FVM), the integral form of the transport equation is obtained as:

$$\frac{d}{dt}\int_V \rho\phi dV + \int_A \rho v\phi \cdot da = \int_A \Gamma\nabla\phi da + \int_V S_\phi dV \tag{3.38}$$

This is composed of a transient, convective flux, diffusive flux, and source term respectively. STAR-CCM+ allows for the user to specify the methods used to discretize the convective and transient terms.

The discretized convective term at a face can be rearranged as:

$$(\phi\rho v \cdot a)_f = (\dot{m}\phi)_f = \dot{m}_f\phi_f \tag{3.39}$$

This requires the values of fluid property ϕ_f at the face. To calculate this value, the central-differencing scheme (CDS) is used. For this scheme the convective flux is defined as:

$$(\dot{m}\phi)_f = \dot{m}_f[f\phi_0 + (1-f)\phi_1] \tag{3.40}$$

where the linear interpolation factor f is defined as:

$$f = \frac{V_1}{V_0 + V_1} \tag{3.41}$$

To discretize the transient term, first order implicit time integration is used. The first order discretization uses the solution at the current time level (n+1), and the previous time level (n) calculated as:

$$\frac{d}{dt}(\rho\phi V)_0 = \frac{(\rho\phi V)_0^{n+1} - (\rho\phi V)_0^n}{\Delta t} \tag{3.42}$$

With the default time step (Δt) being 0.001 s.

3.6 Use of Lagrangian Particles to Represent Air Dissolution

The immiscible fluid treatment of the VOF method means that the simulation will be unable to model bubble creation from dissolution, molecular mixing, and diffusion across the interface. To get around this issue, the bubbles can be modeled as subgrid scale Lagrangian particles dispersed through the domain. To transition the gas from VOF to Lagrangian bubbles the VOF-Lagrangian User Stripping method is used. This model assumes that the stripping is unresolved at a subgrid scale, and instead allows the user to control this transition.

A Lagrangian particle considers the different phase as a discrete point tracked through the continuous medium that it's surrounded by. By analyzing the Lagrangian particle as a discrete moving point, it can be more efficient to solve for the motion of these individual particles, instead of refining the mesh.

This model allows the user to control the stripping by choosing the diameter of the particle, and the mass flux that is changed from VOF to Lagrangian particles. It is assumed that the created particles are spherical. The model uses the volume fraction gradient to calculate the free surface of the fluids, which is where the particles are created. The particles are then created if the flow rate on the surface is large enough to create a parcel with at least one particle, and there is enough mass from the VOF donor phase to create that parcel. The diameter of the particle is limited to 50% of the cube root of the cell volume, and uses the maximum allowable diameter for the cell if the specified diameter is too large.

The stripped parcel is placed at the centroid of the cell on creation. The particle temperature and mass fraction use the values from the VOF phase, while the parcel velocity is determined from the cell velocity. A small velocity perturbation normal to the interface is added to the parcel to push it away from the interface, submerging the bubble under the surface.

The particle uses two-way coupling with the fluid, which allows for the buoyancy and drag experienced by the particle to directly impact the flow field. The drag force acting on the spherical particles is computed based on the work of Schiller and Naumann [34]:

$$C_D = \begin{cases} \frac{24}{Re_d}\left(1 + 0.15 Re_d^{0.687}\right) & 0 < Re_d \leq 1000 \\ 0.44 & Re_d > 1000 \end{cases} \tag{3.43}$$

Where Re_d is the dispersed phase Reynolds number, defined as:

$$Re_d = \frac{\rho_c |v_r| l}{\mu_c} \tag{3.44}$$

where ρ_c is the density of the continuous phase, μ_c is the dynamic viscosity of the continuous phase, and l is the bubble size.

To impose the two-way coupling, the equal and opposite of the forces imposed on the parcels is added to the fluid via source terms. This means that the particles are not directly solved in the VOF continuity equations, but instead their interaction is modeled.

To model the effect of turbulence in the bath on the flow of the particles, a turbulent dispersion model is used. This behavior is modeled using a stochastic approach that includes the effect of instantaneous velocity fluctuations on the particle.

Using the theory derived by Gosman and Ioannides, the particle is assumed to pass through a series of eddies, with eddy time-scale τ_e. Once the particle is determined to have exceeded the eddy-time scale, or the separation between the particle and the eddy is larger than the length scale of the eddy l_e, the eddy returns to the mean value.

The particle is first influenced by fluid velocity v, decomposed as a combination of the mean $\overline{v}$, and the fluctuation:

$$v = \overline{v} + v' \tag{3.45}$$

The velocity fluctuation is considered as a Gaussian deviate with a standard deviation calculated as:

$$u_e = \frac{l_t}{\tau_t}\sqrt{\frac{2}{3}} \tag{3.46}$$

where the turbulence model provides the length of time-scales of turbulence l_t , τ_t. Once the fluctuation is generated, the velocity fluctuation applies until the eddy interaction time is exceeded:

$$\tau_I = min(\tau_e, \tau_c) \tag{3.47}$$

where the eddy time-scale can be related to the diffusion of a passive scalar calculated from the turbulence model used as:

$$\tau_e = \frac{2\mu_t}{\rho u_e^2} \tag{3.48}$$

The Lagrangian bubbles are a modeling proxy, and their effect is limited to removing air from the surface of the cavity, and influencing the fluid flow in the bath. The Lagrangian particles do not resolve any reactions, nucleation, or influence the flow of other bubbles.

3.7 Stagnation Inlets

In the EAF process, the gas is supplied from a pressure tank with a defined stagnation pressure. The velocity of the air exiting the inlet is therefore determined by the expansion properties of the nozzle, and the backpressure of the gas supply. Therefore, it is important to be able to emulate these inlet conditions in the solver, this is done through the use of a stagnation inlet.

The stagnation inlet uses a prescribed total pressure and the absolute static pressure with the isentropic pressure relation to calculate the exit Mach number. This relation is calculated as:

$$\frac{p_t}{p} = (1 + \frac{\gamma - 1}{2}M^2)^{\gamma/(\gamma-1)} \tag{3.49}$$

where p and p_t are the absolute static, and absolute total pressures, γ is the specific heat ratio of air, which is assumed to be constant at 1.4, and M is the Mach number of the flow. The Mach number is then related to the temperature, and velocity at the inlet through:

$$v = Mc = M\sqrt{\gamma RT} \tag{3.50}$$

where v is the velocity, R is the specific gas constant for air, T is the temperature in the cell, and c is the speed of sound.

From these relations the temperature and velocity of the air exiting the nozzle can be calculated using the absolute total pressure and absolute static pressure as boundary conditions.

Chapter 4

Air-Water Interaction

It was previously demonstrated that the EAF method is becoming increasingly popular due to its increased efficiency compared to the BF-BOF method. As steelmakers switch to this process, there is an ever-growing desire to develop a deeper understanding of the process to further increase its efficiencies. One of the main topics of interest is the stirring in the bath, which determines the mixing time in the bath. If a model of the stirring in the bath could be developed, the mixing time could be directly determined. This would save energy that would've been wasted excessively stirring the bath.

To build towards a working model of the stirring from oxygen blowing in the steelmaking process, the computational tools must first be validated on the base physics found in the process. Once validated, the simulation can then be used to build relations between the lance parameters, and the mixing properties in the bath.

To validate the physics of the problem, two different top-blowing impinging air jets onto a water bath are used. The first of which uses a circular jet, which is used to validate tools with the cavity depth relations from Banks and Chandrasekhara [10]. This validation is conducted by varying the stagnation pressure at the inlet, and the height of the lance, and then measuring the respective cavity depth. The second test case uses the planar jet test case conducted by Berger et al. [16]. In this case the velocity fields in both phases are compared along with the shape of the cavity measured in the experiment. Comparing the simulation results with those measured in these experiments will allow for the direct determination of the VOF model's ability to accurately simulate the cavity formation, and mixing imposed by a perpendicular impinging jet.

After validation in this simplified case, additional physics can be added to push the model closer to representing the full EAF blowing process.

4.1 Top-Blown Round Jet

To replicate the cavity depth correlation for the air-jet impinging on water, a model is first developed for the 2D-axisymmetric case. After validation of the cost-effective 2D simulation, the model is expanded to 3D by revolving the axisymmetric geometry around its central axis.

To validate the derived cavity size relations, the cavity response is simulated for lance heights ranging from 0.3m - 1.5m, with inlet stagnation pressures of 10 kPa, 100 kPa, and 1000 kPa. This allows for the cavity validation for all cavity modes described by Molloy [6].

4.1.1 Computational Domain

The domain for the 2D simulations is shown in Figure 4.1. It is composed of wall boundaries colored in black on the right, and bottom edges, a pressure outlet as the upper boundary colored in purple, a stagnation inlet colored in blue, and the axis of symmetry colored in red. To create the geometry for the 3D simulation, the planar geometry is revolved around the red symmetry axis, with the geometric measurements remaining the same.

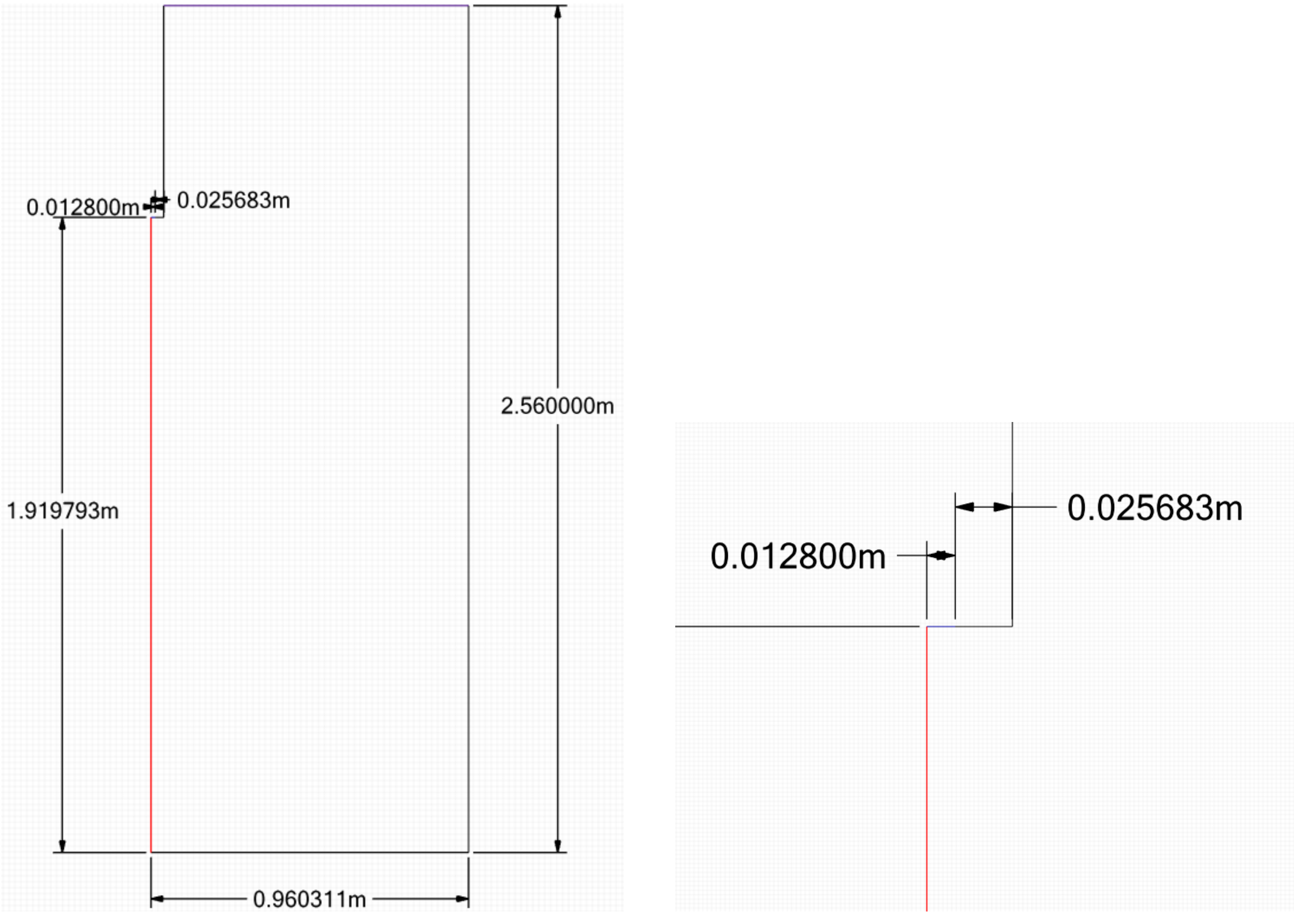

(a) Simulation geometry diagram (b) Closeup view of inlet geometry

Figure 4.1: Schematic of top-blown jet simulation domain

The flow enters from the stagnation inlet, and travels downwards to impact the free surface of the liquid. The height of the jet is controlled by an initial condition that sets the vertical position of the liquid. The size of the domain with respect to the diameter of the jet, allows for a wide range of jet momentums, and blowing heights to be studied without the worry of the influence of boundary conditions on the solution in the cavity.

4.1.2 Mesh

The mesh for both 2D and 3D cases are created from the STAR-CCM+ unstructured polyhedral mesher. The unstructured mesh is chosen due to the complex response of the liquid-gas interface, which would be difficult to capture with a fully structured mesh. As the mesh is refined, the model converges to the computational solution. However, using smaller elements increases computational cost. Therefore, the mesh will be refined in the areas of importance. These are the jet exit, the jet potential core, the jet shear layer, the surface of the interface, and the region around the cavity. To adapt the mesh to the different jet lengths studied, the interface, and cavity mesh refinements are shifted with the height of the liquid such that the interface and cavity would have the same refinement for each simulation, independent of the vertical position.

The list of mesh refinement values relative to the base size is given in Table 4.1.

Region	Jet Exit	Jet Core	Shear Layer	Bath Surface	Liquid Interface	Cavity
Mesh size (% of Base)	3.0	4.0	10.0	40.0	40.0	40.0

Table 4.1: Table of mesh size values

After applying these refinements a global mesh convergence study can be conducted on the mesh to determine if the mesh is sufficiently converged. To monitor the convergence of the mesh, the depth of the cavity for different mesh refinements is observed. The cavity depth is chosen as the convergence criterion because of its importance as a measured quantity, and its sensitivity to the global field. The mesh convergence study is conducted by comparing the depth responses of the base mesh with those of a coarser and finer mesh over a simulation period of 1 second. The base mesh element base size is 0.02m, while the fine and coarse mesh base sizes are 0.015m, and 0.025m respectively. The results of the convergence study are shown in Figure 4.2.

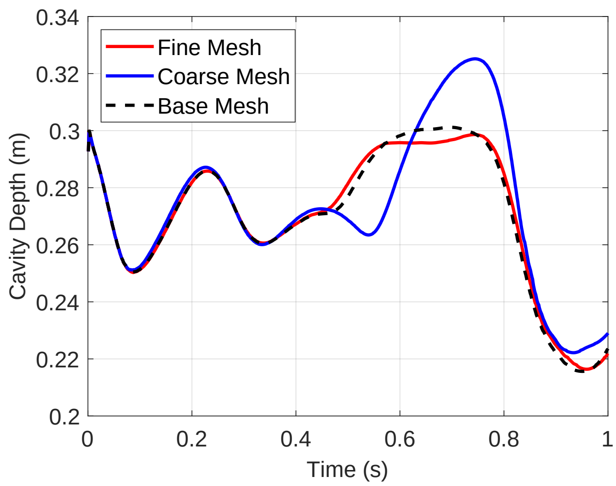

Figure 4.2: Mesh Convergence Study

From the mesh convergence study its shown that the transient depth response is accurately captured using a base size of 2 cm. In the case with a jet height of 50 cm, for the base size of 2 cm, the total mesh count in the 3D domain is 2,480,489 cells, while in the 2D-axi-symmetric domain the total mesh count is 36,075 cells. A planar section of the mesh for this case is shown in Figure 4.3.

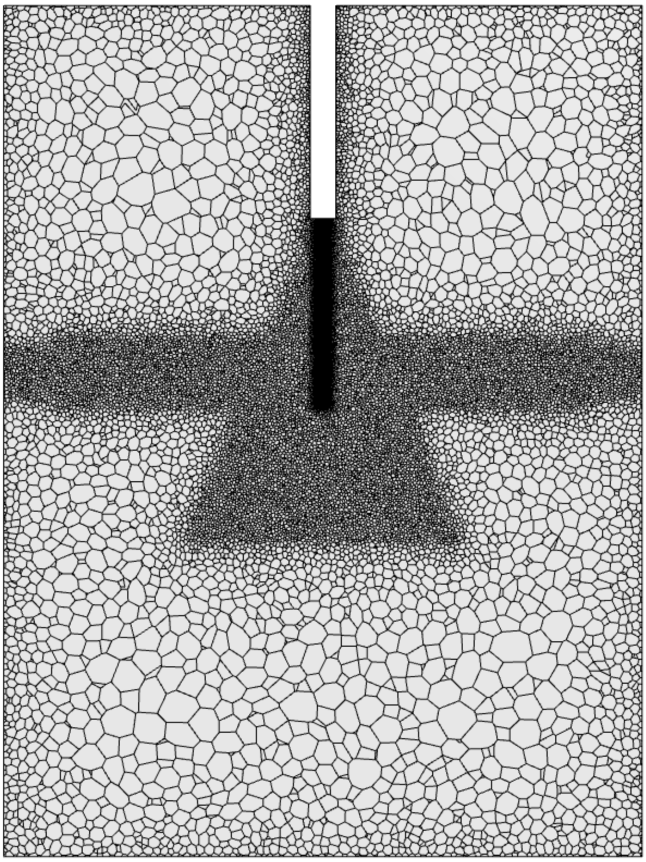

Figure 4.3: Mesh used for a lance height of 50 cm

4.1.3 Results

After proving that the utilized mesh ensures convergence to the computational values of interest, the results of the 2D and 3D cavity response can be compared to the correlations derived in the literature. The quantities of interest of this study are the depth of the cavity, and how this depth changes over time. This is done by establishing the 2D-axisymmetric results as a baseline which is then used as a reference result for the expansion into 3D.

The first subject analyzed is the depth of the cavity for the different height-pressure configurations. The simulations were first conducted in the 2D-axisymmetric case where the lance height was varied from 0.25 m to 2.5 m, with steps of 0.25 m. For these cases three pressure values were considered, 10 kPa, 100 kPa, and 1 MPa, which with isentropic expansion from the stagnation inlet yields respective jet core velocities of 125 m/s, 323 m/s, and 540 m/s. Next the simulation is scaled up to 3D, where a selection of 6 of the 2D cases are analyzed covering the dimpling, splashing and penetrating cavity modes. This subsection allows for the model to be validated across the different cavity-related phenomena, while also keeping the computational time to a minimum. The depth values retrieved from the simulation, are then compared with the analytical expressions derived by Banks and Chandrasekhara [10]. The depth results for the different lance heights, and pressures studied are shown in Figure 4.4.

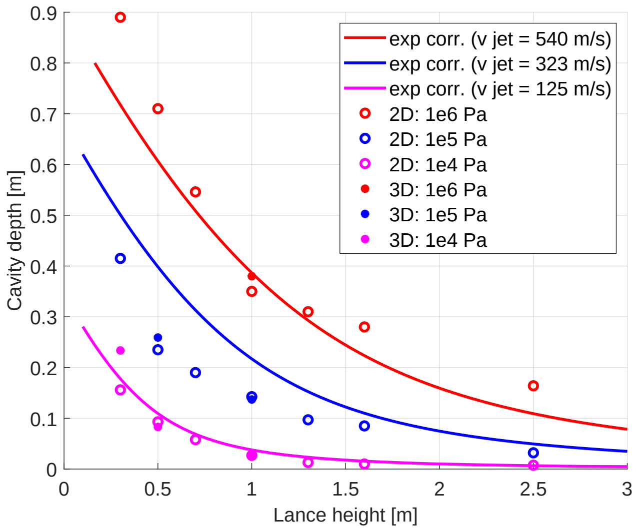

Figure 4.4: Measured Cavity Depth for different inlet pressures, and lance heights

Analyzing the data reveals that the 2D-axisymmetric and 3D simulations generally match the expected depth derived from the analytical correlation for the different height and pressure configurations. The different simulation results follow the expected trend, with the cavity depth trending inversely with the height of the jet, and the cavity depth increasing with the velocity imposed by the total pressure at the inlet.

However, the proximity of the simulated values to the analytical values noticeably shifts between the different imposed inlet pressures. For the lowest pressure, 10kPa, the depth of the cavity is accurately predicted by the 2D-axisymmetric, and 3D simulations for the entire range of lance heights studied. Meanwhile for the 100 kPa case, the depth is considerably under-predicted for the 2D-axisymmetric and 3D simulations, with the discrepancy growing inversely with the height of the lance. This trend does not continue as the inlet pressure is increased to 1 MPa, where the simulation over-predicts the depth of the cavity. However, for the two inexact pressure configurations the inaccuracy of the cavity depth becomes more noticeable as the lance height decreases.

Another essential quality to analyze is the time-response of the cavity captured by the 2D-axi-symmetric, and 3D simulations. By comparing the transient results, the additional instabilities in the cavity that are introduced as a result of switching the simulation into 3D can be analyzed. This can help develop a better understanding of what is important to take note of when analyzing the full 3D cavity.

The first quantity compared is the depth of the cavity, and how it evolves over the simulation time. The simulation is initially run until the cavity depth is established, and is in stable oscillations. From this state the depth results over a 5 second simulation window are compared for a lance height of 0.5 meter, and a inlet total pressure of 100 kPa. This configuration is chosen for a more detailed analysis because it most closely matches the cavity response that is predicted in the full EAF process. In the EAF process the lance has an exit stagnation pressure on the order of 1e6 Pa, and a jet height of 1.5 to 2 meters. Analyzing the depth trends from Figure 4.4 shows that these EAF conditions produce a similar cavity depth to that of the 0.5 m height, 100 kPa stagnation pressure case. This decreased case is chosen to reduce the number of elements in the mesh, and to reduce the velocity of the flow to maintain stability with the segregated pressure solver. The transient depth results for the two simulations, along with their time averaged values are shown in Figure 4.5.

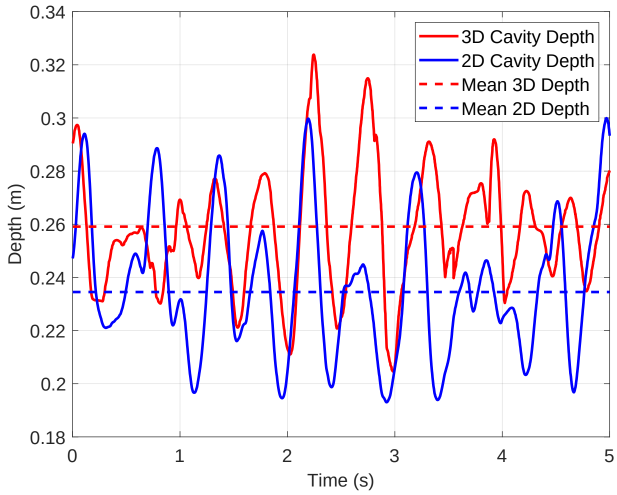

Figure 4.5: Comparison of cavity depth response for the 2D-axisymmetric and 3D simulations

One interesting quality is that the 2D-axisymmetric depth is considerably smaller than in the full 3D case. This discrepancy shows that there are some aspects of the physics that are not captured in the 2D case as a result of this boundary condition, therefore as more complex models are added it would be best to continue with the more expensive 3D simulation. Analyzing the transient depth plot shows that the cavity is heavily oscillatory for this specific blowing condition, which follows the prediction from Molloy for the penetrating cavity mode [6]. In both the 2D, and 3D cases the cavity depth oscillates to upwards of 20% of its mean depth value. It is interesting to note that the 2D cavity exhibits the same order of oscillation as the 3D cavity with less possible variability due to the axisymmetric boundary condition that is applied to the center of the cavity.

To better analyze the oscillatory behavior of the cavity depth for the two simulations, an FFT is conducted on the transitory depth responses. These transforms are shown in Figure 4.6.

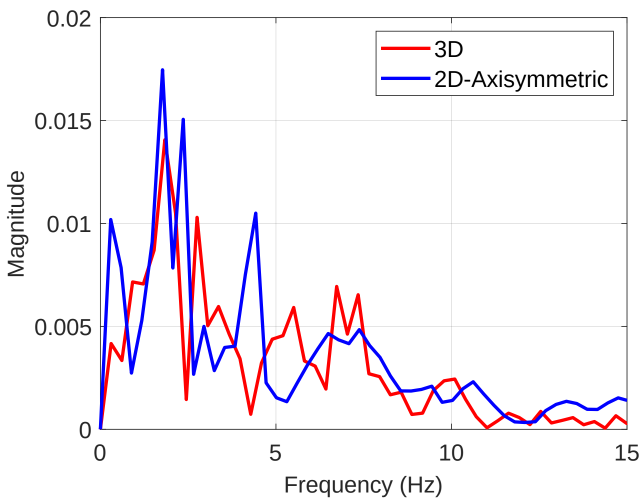

Figure 4.6: Comparison of cavity depth FFT response for the 2D-axisymmetric and 3D simulations

The Fourier transforms show that the oscillating frequencies are very similar for the 2D and 3D cases. It can also be shown that there is no principal oscillation frequency in the simulations, but instead that the cavity depth oscillates mostly below 5 Hz, with a secondary smaller peak near 6-7 Hz. This doesn't exactly match what was observed experimentally, where there is a clear peak in the data. The general oscillation frequency is at the low end of the general 4-12 Hz range found in the literature [32].

Although the 2D axisymmetric case is able to achieve comparable results in terms of the cavity depth, the imposed axisymmetric condition removes instabilities and other potential transient behavior from the cavity. This boundary condition allows the cavity to be more accurate for values that are near this axis of symmetry. One such value, is the maximum depth of the cavity, which is located near the center-line of the jet as the maximum momentum reaching the surface is in the jet-potential core. However, as one goes radially outwards from the jet, the instabilities compound and quantities like the shape of the cavity can no longer be considered instantaneously symmetric. Instead the cavity shape is found to vary instantaneously with regards to its orientation, but due to the symmetry of the geometry, it can be considered statistically axisymmetric.

This cavity variance can be shown clearly by analyzing an instantaneous cut of the cavity profile for the 2D, and 3D simulations.

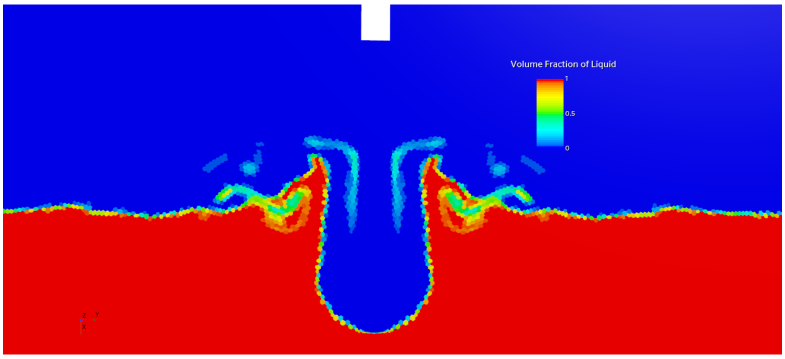

(a) 2D-Axisymmetric

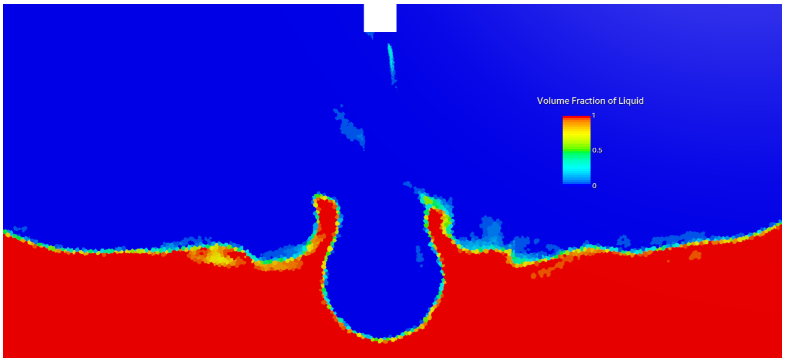

(b) 3D - XY Plane

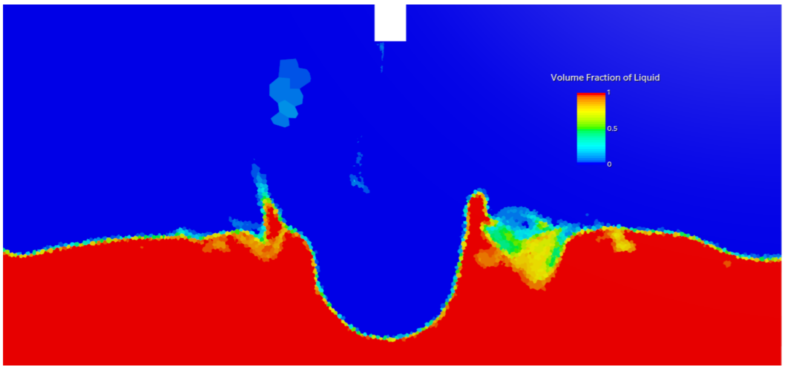

(c) 3D - XZ Plane

Figure 4.7: Comparison of instantaneous cavity shapes for the H = 50 cm, P0 = 100 kPa case

Comparing the planar slices of the instantaneous cavity profiles shows that the shape of the 2D cavity is noticeably different compared to that of the 3D cavity. The 2D cavity is noticeably steeper, and the symmetric boundary condition induces nonphysical splashing effects. Another distinguishing feature between the 2D and 3D simulations is the instantaneous asymmetry of the cavity, which is clearly shown comparing the responses shown in Figures 4.7b, and 4.7c. This asymmetry of the cavity imposes an additional challenge when trying to measure the average shape of the cavity.

To get an accurate measure of the shape of the cavity, the time averaged shape must be measured for the different simulations. However, in the 3D case the spatial average must also be taken due to the instantaneous variance in the cavity shape. The cavity in the 3D case can be considered statistically symmetric due to the boundary conditions, and jet blowing being symmetric about the central jet axis. Therefore, to get an accurate measure of the average cavity shape in time, and orientation, the cavity is discretized into different radial measurements, which are averaged over the simulation time. The cavity radius is measured at 8 different points angularly spaced by 45°, while for the 2D case the radius is only measured once, directly from the axis of symmetry. These radial values are measured at 11 equally distributed depths, spaced by 2cm from the surface of the bath to 20 cm below the unperturbed interface. This, along with the average depth of the cavity, yields 12 discrete points that can be used to characterize the mean shape of the cavity. This measurement technique is visualized in Figure 4.8.

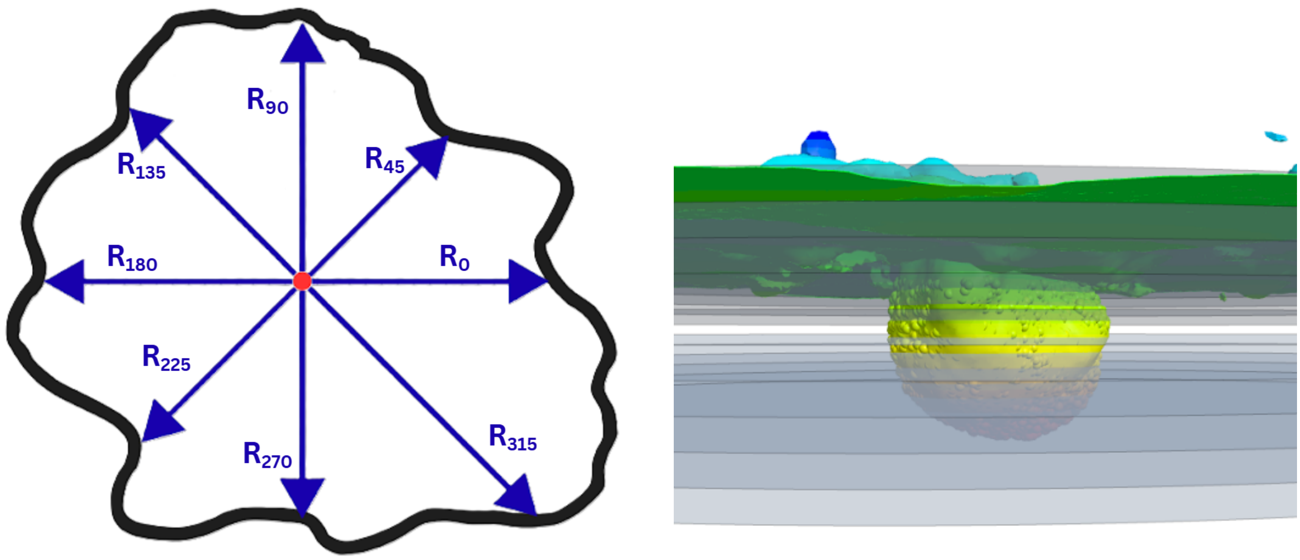

(a) Radial Measurement Method (b) Depth Measurement Method

Figure 4.8: Methodology used to measure the shapes of the cavities

After measuring the different mean radius values, the results for the 2D-axisymmetric, and 3D simulations are compared in Figure 4.9.

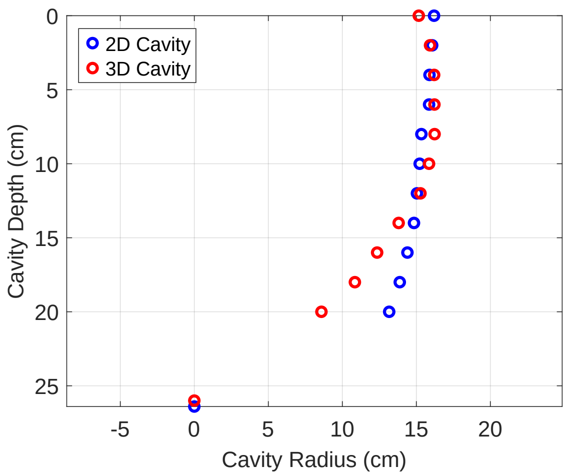

Figure 4.9: Comparison of cavity shapes for the 2D and 3D simulations

Analyzing the two mean cavity shapes confirms that the 2D axisymmetric cavity is much steeper than the 3D cavity, with the discrepancy in the slope being much more prominent near the bottom of the cavity. To determine the physicality of the different responses, the different cavity shapes can be compared to the elliptic and parabolic shapes that were measured by Banks and Chandrasekhara [10]. The elliptic and parabolic fits for the two simulations are shown in Figure 4.10.

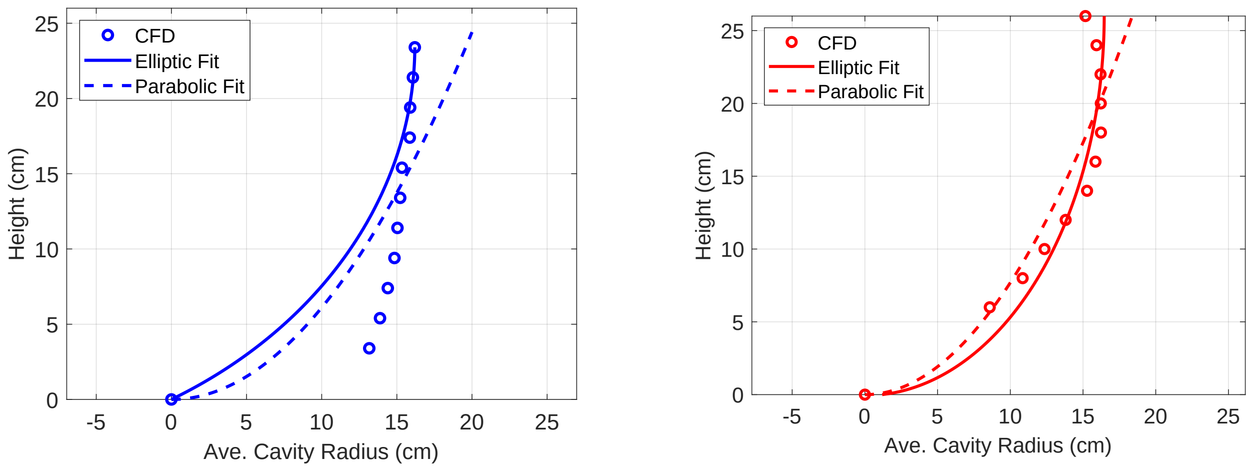

(a) 2D Cavity shape curve fits

(b) 3D Cavity shape curve fits

Figure 4.10: Elliptic and parabolic curve fits for the 2D and 3D cavity shapes

The steepness of the cavity in the 2D-axisymmetric case does not match either of the theoretical cavity predictions, with the bottom of the cavity being tapered much less than predicted. The 3D cavity matches better with both predictions, with the elliptic fit being a closer match to the measured shape of the cavity. This compares well with the elliptical shape prediction for deep cavities formed by Evestedt and Medvedev [26]. Overall, the shape measurements of the cavity show that the cavity from the 3D simulation matches closely with theory, while the cavity from the 2D-axisymmetric simulation produces a shape that isn't supported by previous experimental results.

To conclude, the simulations of a cold round jet impinging onto a water surface are conducted for stagnation pressures of 10 kPa, 100 kPa, and 1 MPa, and lance heights ranging from 0.3 m to 2.5 m. The simulations are run in 2D-axisymmetric, and 3D geometries, with the depth results being compared with the analytical expressions derived from experimental results measured by Banks and Chandrasekhara [10]. The depths measured in the 2D axisymmetric, and 3D simulations were found to match well with the analytical predictions for both the 2D, and 3D cases. After validating the cavity depths, the shape of the cavity was measured for a stagnation pressure of 100 kPa, and a lance height of 50 cm in both the 2D axisymmetric and 3D cases. This case was chosen because it predicted a cavity shape similar to the shape found in the EAF furnace. The shape of the cavity in the 3D simulation was found to match closely with the elliptical prediction from Evestedt and Medvedev [26], while the shape of the cavity from the 2D shape did not match either the elliptical or parabolic shapes predicted in the literature.

4.2 Mixing from a Top-Blown Jet

To replicate the experiment conducted by Berger et al. [16], the nozzle geometry, boundary conditions, and inlet conditions are copied for the dimpling cavity regime. The inlet conditions producing the dimpling regime are chosen due to the predicted stability of the cavity for this regime by Molloy [6]. The stability of the cavity will allow for a more direct comparison of the velocity fields, and cavity shape due to the fact that they will not have to be time averaged. The cavity parameters, and velocity fields are measured on a planar section in the middle of the domain to remove any impacts from the boundaries on the simulation.

4.2.1 Computational Domain

To reproduce the experimental setup, the nozzle geometry, nozzle height, and water depth are kept constant between the simulation and the experiment. However, the width, and depth of the domain have been shrunk to reduce the cost of the simulation. The velocity, and cavity shape are measured on a plane in the center of the domain, normal to the line jet. However, the simulation is conducted in 3D due to the aforementioned discrepancies in the cavity formation seen in 2D simulations. The computational domain for the simulation is shown in Figure 4.11, with the green region representing the inlet, the red area representing the gas region, and the blue area representing liquid region. The bottom, and all 4 sides of the domain are considered no-slip wall boundaries, while the top boundary is broken into the green velocity inlet, and the red pressure outlet. The inlet is set as a velocity inlet with an exit velocity of 6.0 m/s, and turbulence intensity of 0.04. The outlet is set as a pressure outlet with an ambient static pressure of 101325 Pa. The temperature in the domain, and for the boundaries is set as 300 °K. The properties of the different fluids are given in Table 4.2.

Fluid	Density (kgm^{-3})	Dynamic Viscosity (Pa-s)	Surface Tension (Nm^{-1})
Air	1.225	1.855E-5	-
Water	1000	8.887E-4	0.072

Table 4.2: Properties of fluids used in the simulation

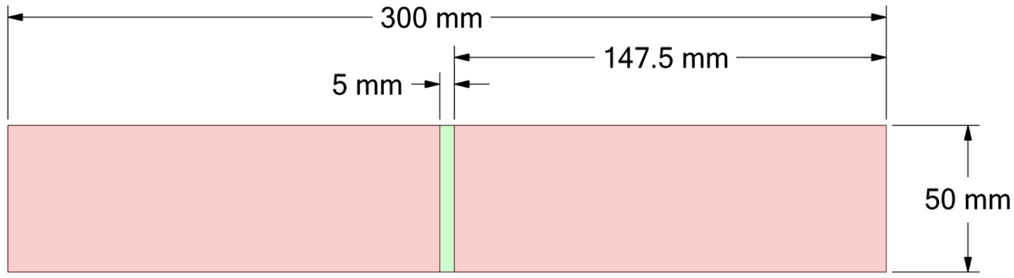

(a) Top view of geometry

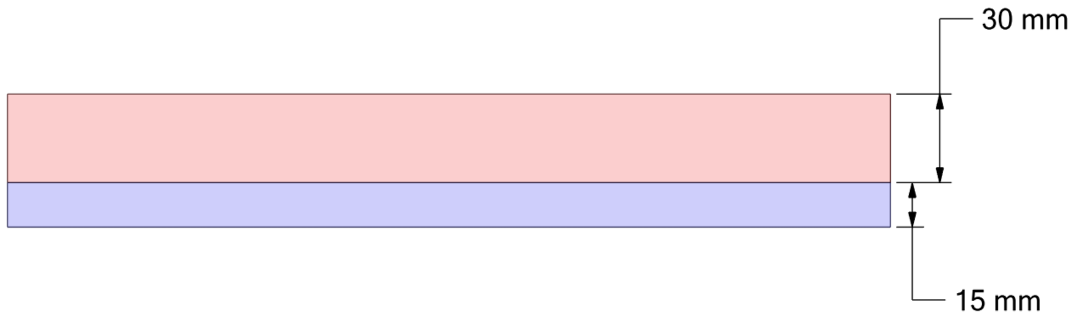

(b) Front view of geometry

Figure 4.11: Schematic of geometry used

To create the mesh, mesh controls were added to refine the jet region, the region around the cavity, and the interface between the gas and liquid phases. The different mesh refinement regions are shown in Figure 4.12a. For the mesh refinements, the red shaded regions were set to 20% of the mesh base size, while the blue region was set as 7.5% of the base size, with the mesh base size being set at 2 mm. These planar mesh controls are constant across the depth of the domain yielding a total element count of 6,928,688.

(a) Mesh refinement regions

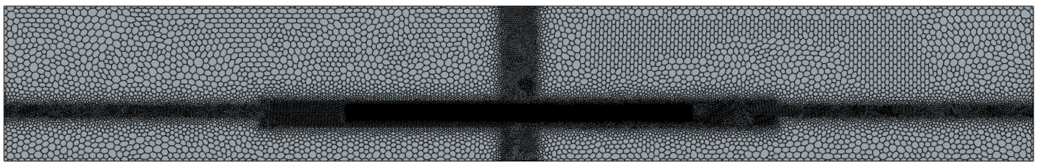

(b) Final mesh

Figure 4.12: Mesh for Bath Mixing Simulation

4.2.2 Results

To be able to compare the results between the experiment and the simulation, the assumption that the cavity is steady must first be confirmed. This would then allow instantaneous cavity and velocity magnitude field values to be compared directly with the experimental results, without needing to time-average. To assess the steadiness of the fluid response, the cavity depth in the unsteady simulation is recorded and shown in Figure 4.13.

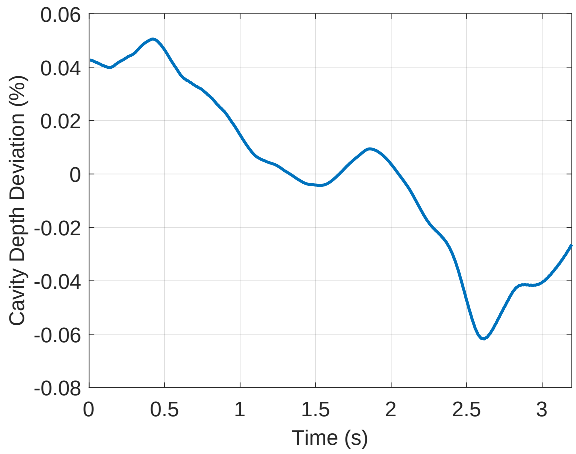

Figure 4.13: Percent temporal variation in cavity depth response

The unsteady cavity depth is shown to vary on the order of ± 0.1 %. This shows that the cavity is stable in the dimpling regime, which matches the theory of Molloy [6]. This stability allows for the instantaneous field variables to be used to analyze the cavity response, which are then compared with the experimental results.

First the cavity shape is compared between the simulation and experiment to get a clearer analysis of the VOF model's ability to capture the deformed interface. This is shown in Figure 4.14. The simulation result is found to match the experimental cavity measurements quite well in the cavity depression itself. However, after reaching the lip of the cavity, around x/b = 3, the simulation diverges slightly from the experimental result. Here the experimental result shows the interface returning to the unperturbed height, while the simulated interface dips slightly. Overall, the simulation is shown to accurately capture the size, and shape of the cavity for this steady configuration.

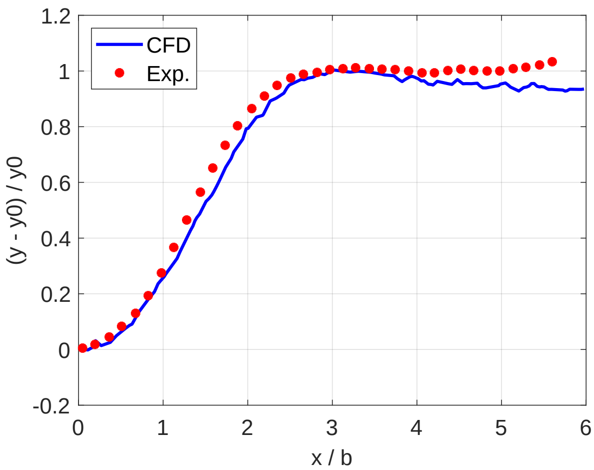

Figure 4.14: Cavity profile comparison

After the cavity profile is confirmed to match, the velocity fields in the gas, and liquid can be compared to determine the accuracy of the VOF model in simulating the mixing produced by an impinging jet. First the air velocity is compared, shown in Figure 4.15, with the experimental results shown on the left, and the simulation results on the right. The colorbar shown is the same for both fields. The simulated velocity distribution is shown to closely match that of the experiment, with the stagnation region near the center of the cavity, and the acceleration around the cavity lip both being clearly captured. However, one discrepancy to note is the magnitude of the velocity, with the simulated result being a slight under-prediction of the experimental field.

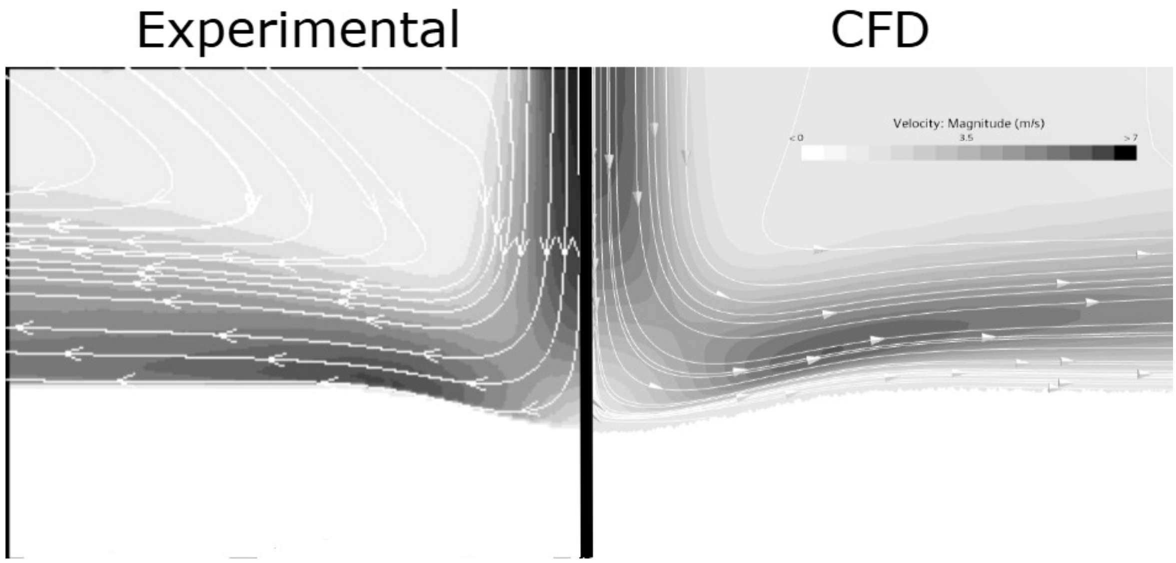

Figure 4.15: Air Velocity magnitude field comparison

The velocity field in the bath shows general agreement in magnitude, and structure. The vortex located beneath the lip of the cavity is shown to be in a similar location, and the strength of the vortex matches well between the two simulations. One noticeable difference is the location of the peak velocity in relation to the liquid surface. In the experimental velocity field, the maximum velocity is shown to be much nearer to the surface than the simulation results. This peak velocity is also shown to be slightly higher than the peak velocity from the VOF method. This interface discrepancy can be important to note for future work. For example, if chemical reactions or other surface effects are added, inaccuracy of the model at the interface can cause discrepancies between the physics, and the simulation results.

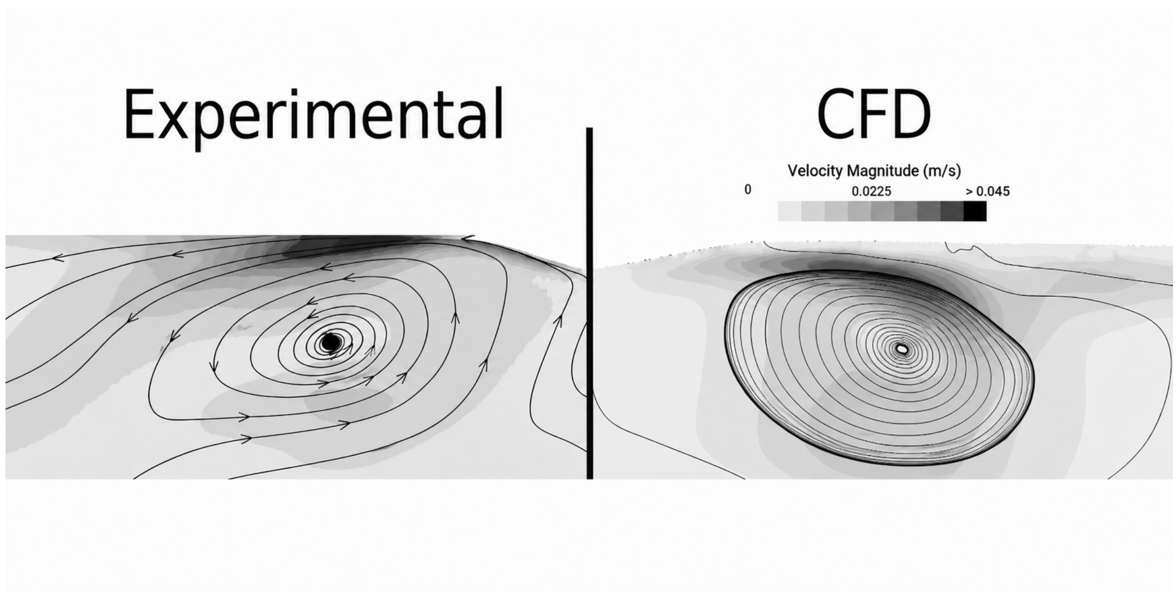

Figure 4.16: Water velocity magnitude field comparison

To conclude, the vertical impinging line-jet experiment conducted by Berger et al. [16] was recreated in a reduced domain. The results were reproduced for the dimpling case with Reynolds number Re = 2000. The flow fields in the liquid and gas around the cavity, along with the shape of the cavity were measured at the mid-plane of the domain, and compared with the experimental results.

It was found that the velocity fields from the simulation were overall a good match with the measured fields from the experiment. The gas-phase velocity was slightly underpredicted by the simulation, and the liquid phase velocity underpredicted the velocity near the liquid-gas interface. The shape of the cavity was found to match well between the simulation and experiment with a slight discrepancy away from the cavity.

Overall the VOF method was found to be able to accurately predict the flow fields, and cavity shapes induced by vertical impinging jets.

Chapter 5

Emulation of the Oxygen-Molten Steel Interaction

The VOF model has been validated for simplified models of impinging air jets onto water surfaces. However, more complex physics arise in the EAF process, where chemical reactions and high temperatures play an influential role in the surface deformation characteristics imposed by the impinging jet. One of these key interactions is the stirring induced by bubbles in the bath. It has been found that bubbles can increase the stirring in the furnace by up to an order of magnitude [35]. Therefore, it is important to attempt to model these effects, so the stirring in the bath can be more accurately characterized.

However, the VOF model treats fluids as immiscible, and resolving the micro-scale bubbles is too expensive. Therefore, Lagrangian air bubbles are created at the liquid-gas interface, and their effect on the cavity is studied. The use of Lagrangian bubbles allows the size, quantity, and removal of the bubbles to be directly specified, which allows for more control over the simulation.

5.1 Case Setup

To directly study the impact of the bubbles, the previously used 3D top-blown jet geometry is used for the lance height of 50 cm to recreate the EAF cavity conditions. This allows for the bubbling results to be directly compared with the previous measurements, with the same cavity measurement methods. The geometry is shown in Figure 5.1.

To determine the impact that the bubbles have on the bath, 3 different bubbling conditions are imposed. The first condition is a baseline condition, where no bubbles are created. The second condition creates the bubbles at the interface, and removes them at the next time step to analyze the effect of mass stripping on the surface of the cavity. The third condition creates the bubbles at the interface and only removes them after they reach the surface of the liquid, this allows for the analysis of the impact of the movement of the bubbles on the cavity. The bubbles are created at two different mass fluxes, equal to 50% of the inlet mass flux, and 100% of the inlet mass flux, which aims to simulate different reaction rates at the cavity surface.

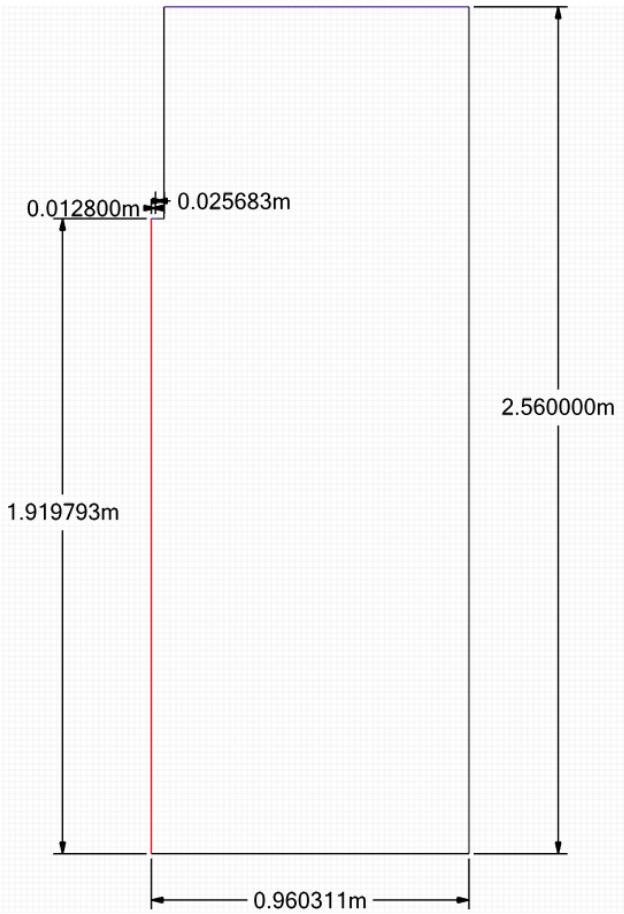

(a) Schematic of domain used for analysis of Lagrangian bubbles

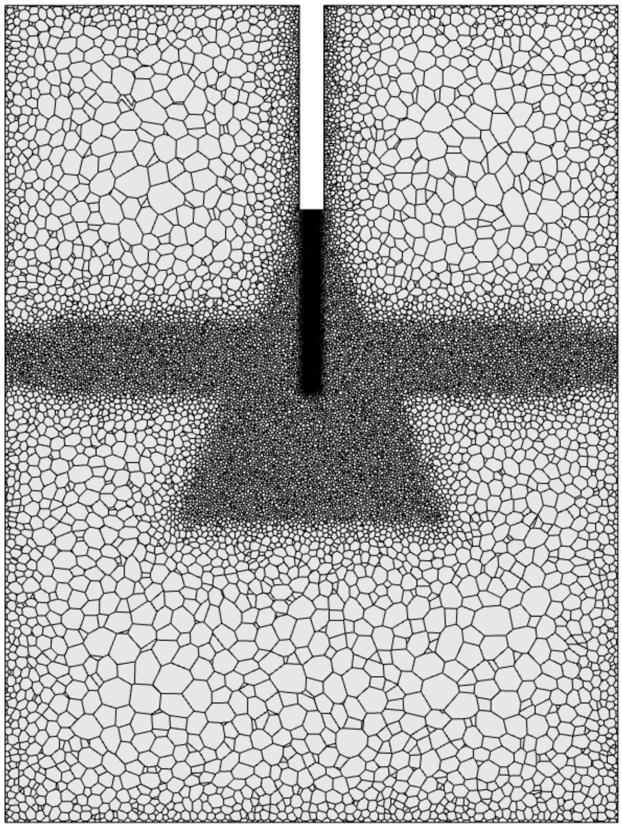

(b) Image of mesh used in Lagrange simulation

Figure 5.1: Schematics of domain geometry and domain mesh in the bubble modeling cases

The mesh used in this simulation uses the same converged mesh controls from the previous 3D water model. An image of the final mesh is shown in Figure 5.1b.

5.2 Results

First the distribution of bubbles in and around the cavity for the different bubble conditions can be analyzed, shown in Figure 5.2. In the removed cases it can be seen that the bubbles are only seen directly on the cavity surface, with the higher mass stripping case having a denser distribution of bubbles. In the cases where the bubbles are maintained, we can see that the bubbles spread across the entire liquid domain, but the majority of the bubbles remain near the cavity. In the 100% maintained case there are bubbles that reach further from the cavity, however the general distribution of bubbles is similar.

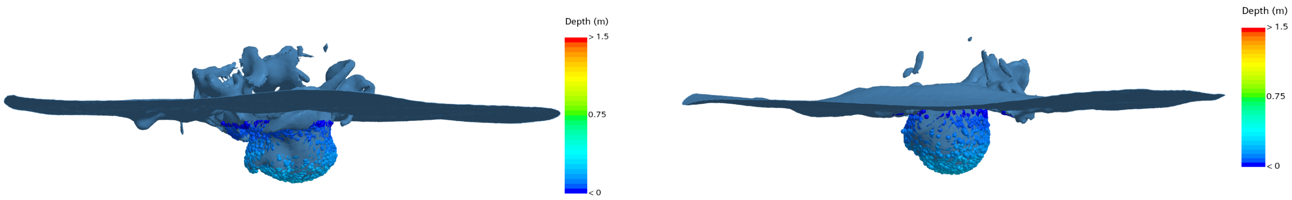

(a) 50% Removed (b) 100% Removed

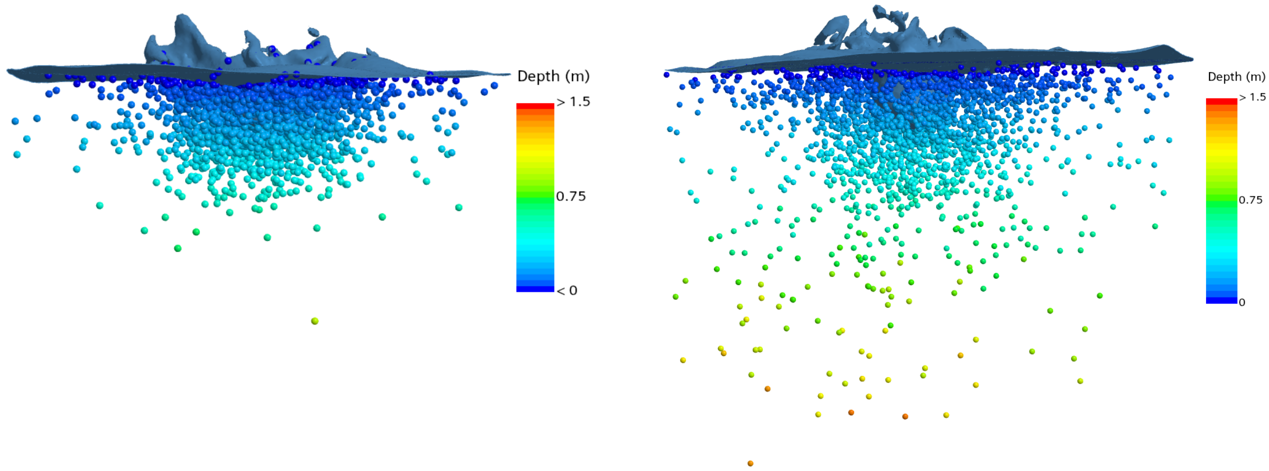

(c) 50% Maintained (d) 100% Maintained

Figure 5.2: Images of instantaneous bubble distribution for the different bubble creation conditions

To run the simulation for the different bubble cases a common base simulation was run where the pressure was increased to 100 kPa, and the simulation was run until the cavity was in steady state oscillations. From this base case the bubbles were added using the different conditions.

To measure the mean cavity values, only the depth, area, and volume values after this change to bubbling conditions are used. The depth response of the simulation before and after the bubbles are added are shown for the 50% removed case in Figure 5.3.

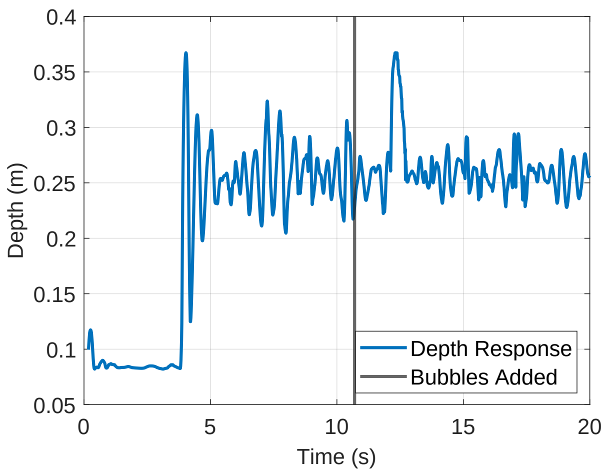

Figure 5.3: Example of transient depth response before and after adding bubbles

The effect of the different bubble creation conditions on the cavity geometry can be studied. This is done by analyzing the transient depth, surface area, and volume responses of the cavity. These responses are shown in Figures 5.4, 5.5, 5.6. The time used in these responses is the time after the bubbling conditions were changed.

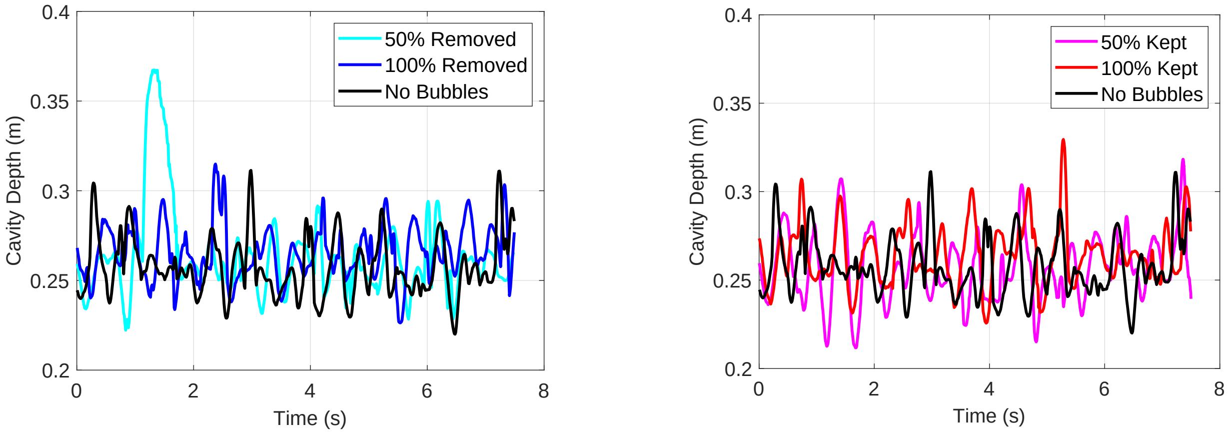

(a) Cavity depth for removed bubbles

(b) Cavity depth for maintained bubbles

Figure 5.4: Transient cavity depth response for the different bubble conditions

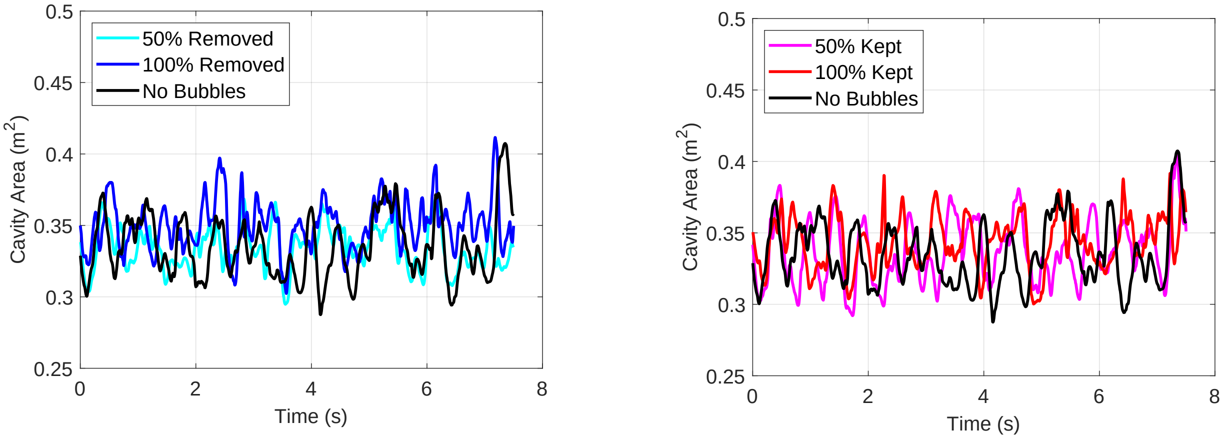

(a) Cavity area for removed bubbles

(b) Cavity area for maintained bubbles

Figure 5.5: Transient cavity surface area for the different bubble conditions

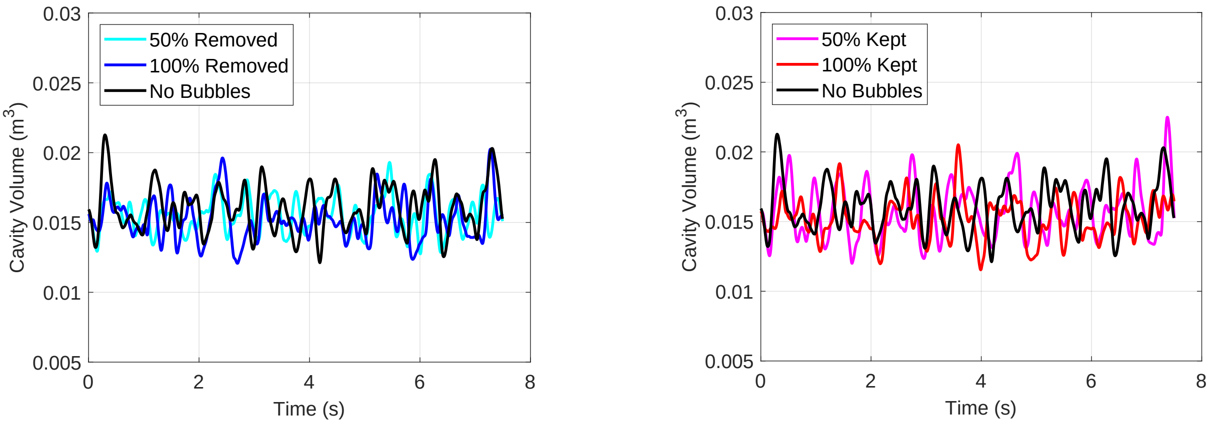

(a) Cavity volume for removed bubbles (b) Cavity volume for maintained bubbles

Figure 5.6: Transient cavity volume for the different bubble conditions

Visually analyzing transient geometric responses shows that the cavity responses for the different bubbling conditions are similar to the base case. The different geometric parameters in the bubbling cases oscillate similarly to the base case, with similar magnitudes. However, the mean depth, area, and volume can be calculated to reveal the effects of bubble creation on the cavity. These mean results are shown in Table 5.1.

	No Bubbles	50% Removed	100% Removed	50% Kept	100% Kept
Average Depth (m)	0.2577	0.2636	0.2657	0.2559	0.2642
Average Surface Area (m^2)	0.3349	0.3342	0.3501	0.3387	0.3438
Average Volume (m^3)	0.0161	0.0155	0.0152	0.0158	0.0152

Table 5.1: Averaged cavity dimensional parameters for the different bubble creation conditions

Analyzing the cavity geometries in Table 5.1 reveals that the different bubble conditions have a measurable impact on the size of the cavity, but this result is relatively small. The largest depth difference with respect to the base case is 0.8 cm, which is 3.1% of the total depth. While the largest surface area, and volume differences are 4.54%, and 5.92% respectively. One trend to note is that most bubbling cases have a deeper cavity, while the volume of the cavity decreases as the mass stripping is increased. This, along with the larger difference in volume reveals that the depth of the cavity isn't heavily influenced by the creation of bubbles, but instead the shape of the cavity is what is impacted most.

The shape of the cavity can be analyzed using the same radial measurement system as before due to the same symmetry condition, and similar cavity sizes. First, the different cavity shapes for the same bubble creation rate are compared with the baseline cavity shape to determine the impact of the bubble removal on the shape of the cavity. These cavity profiles are illustrated in Figure 5.7.

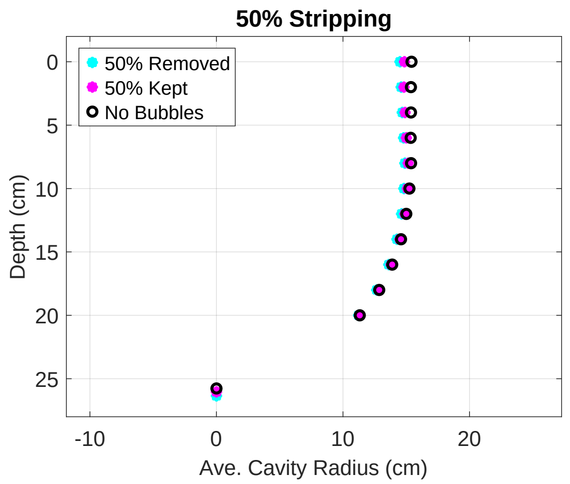

(a) Cavity shapes for 50% bubble cases

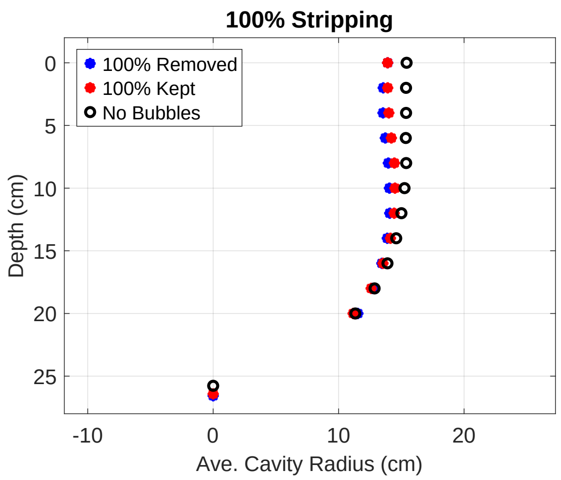

(b) Cavity shapes for 100% bubble cases

Figure 5.7: Cavity shape comparison between the different bubble conditions

Analyzing the different cavity profiles in Figure 5.7 reveals that the cavities in the bubbling cases are radially smaller than the baseline case, with the difference becoming more pronounced closer to the surface. It is also shown that as the mass creation rate of bubbles is increased, the radius of the cavity gets smaller. Comparing the different bubble removal conditions shows that the difference in cavity radius is smaller than the difference between the different bubble conditions and the baseline. However, the cases with removed bubbles are noticeably smaller than the cases with the maintained bubbles. This could potentially be explained by the non-conservative removal of the bubbles' mass, compared with the conservative treatment of the Lagrangian parcels until they reach the surface, which can occur away from the surface of the cavity. However, in the maintained bubbling condition, the bubble removal process can still happen on the surface of the cavity if that is the first interface that the bubble reaches.

The shapes of the different cavities can then be compared through curve fits through the radial data points. From the previous results it was shown that this blowing case yields a more elliptical cavity shape, so only the elliptical curve fits are compared. These shapes are compared between the different mass stripping rates for the same bubbling conditions, as the difference in mass stripping rate was shown to have a larger impact on the shape of the cavity. These elliptical curve fits are compared in Figure 5.8.

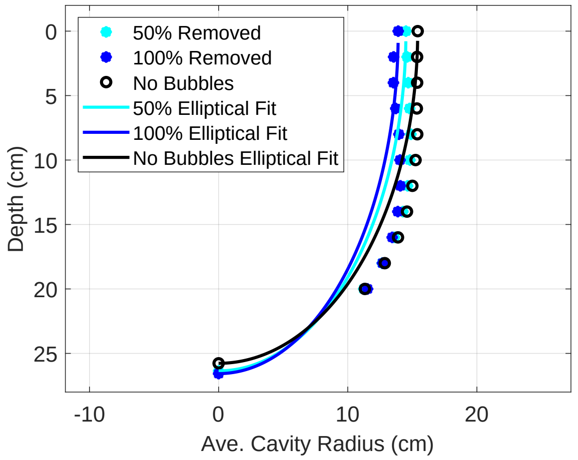

(a) Cavity shapes and curve fits for removed bubble conditions

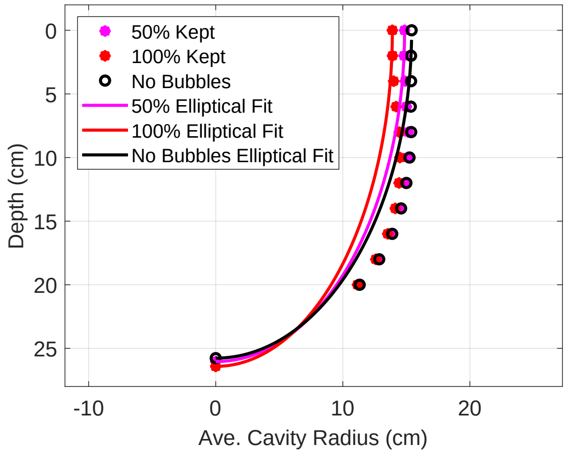

(b) Cavity shapes and curve fits for maintained bubble conditions

Figure 5.8: Cavity shapes and curve fits for the different bubble conditions

The cases with higher bubble creation rate are shown to have smaller radii than the lower creation rate cases, and the baseline. This effect is clearer in the shallower parts of the cavity, with there initially being very little difference near the bottom of the cavity. The effect of a larger depth, and lower radii makes the cavities with higher bubble creation rates much narrower compared to the baseline cases, which is clearly shown in the elliptical curve fits. These smaller shallow radial values cause the cavity to diverge from the more elliptically shaped baseline case. Overall the change in the cavity radius values are small with the largest difference being 1.5 cm. However, this is still a 9.21% difference from baseline, which is a considerable change to the shape of the cavity near the surface.

The transient response of the cavity in the different bubble conditions can then be analyzed by conducting FFTs of the depth responses. These results are shown in Figure 5.9.

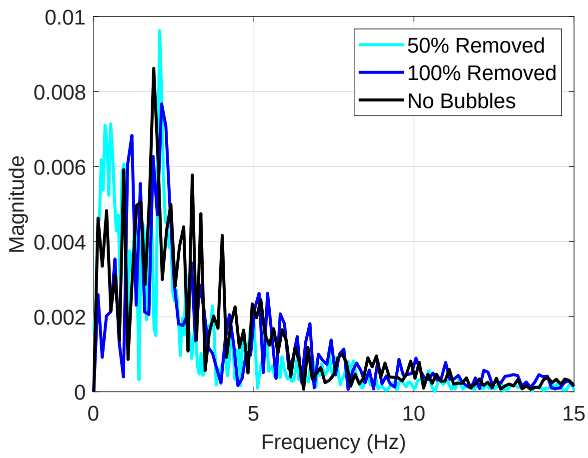

(a) FFT comparison for removed bubble conditions

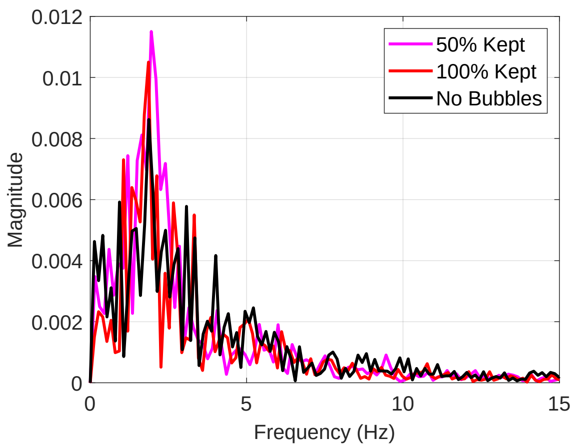

(b) FFT comparison for maintained bubble conditions

Figure 5.9: FFT comparisons of the different bubble conditions

The FFT responses show very little difference between the different bubble conditions, with a main frequency peak of 2 Hz being visible for all of the conditions. Thus, the bubbles have very little impact on the oscillatory behavior of the cavity, but most of their impact instead comes through the change in shape.

To conclude, the creation of bubbles due to chemical reactions in the EAF process was emulated using Lagrangian bubbles that were created by stripping mass from the gas phase at the interface of the cavity. To analyze different effects of the bubbles two bubble mass creation fluxes were used, equal to 50%, and 100% of the mass flow from the stagnation inlet. The bubbles were also analyzed for two different bubble removal conditions, one where they were removed one time-step after creation, and one where the bubbles were removed upon reaching the liquid-gas interface after being submerged.

It was found that the creation of bubbles from mass stripping had a small, but noticeable impact on the shape and depth of the cavity. The creation of bubbles was found to deepen the cavity by up to 0.8 cm, and reduce the radius of the cavity at the bath surface by up to 1.5 cm. The difference in cavity shapes between the two bubble removal conditions was small compared to the difference in cavity shapes between mass stripping rates.

Chapter 6

Real Process Replication

After validating the simplified VOF model for impinging jets, another step can be taken towards representing the EAF process by emulating the blowing conditions found inside the furnace. However, due to the high complexity involved with modeling the chemical reactions and high temperatures in the furnace, a simplified, representative model of the blowing conditions in the furnace is desirable. It has been found that the momentum of the jet reaching the bath is comparable for the standard supersonic jet and coherent jet in the potential core region. This effect is also seen when comparing standard supersonic jets in hot and cold temperatures. Therefore, to emulate the blowing conditions in the furnace, a lance with a stagnation pressure similar to those seen in the EAF process, can be positioned such that the potential core reaches the bath surface. This allows for the analysis of the cavity formed, and the flow induced in the bath, which can then be validated using real EAF conditions.

6.1 Case Setup

In choosing conditions for the nozzle, it is important to be able to directly compare the results between the standard supersonic jet, and coherent supersonic jet. With the added complexity that comes with modeling the coherent jet, it is also important to choose nozzle conditions and geometries that align with previous work. This allows the coherent jet simulation to be validated on its own before being added to the VOF simulation. This ensures coherent jet blowing is accurate, and can be compared to the blowing from the standard supersonic jet. Therefore the conditions of the lance are chosen to mimic coherent jet research by Tang et al. [17]. The geometry of their nozzle is shown in Figure 6.1.

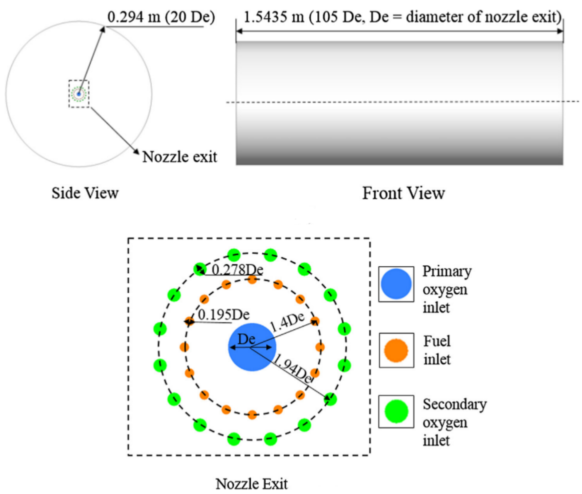

Figure 6.1: Geometry of nozzle used in coherent jet simulation [17]

To modify the nozzle for use as a standard supersonic jet, the secondary inlets used for oxygen and CH4 are closed so only the primary inlet remains with the same overall lance width. The inlet conditions for the primary nozzle are a stagnation pressure of 929000 Pa, and a total temperature of 294 K. The radius of the primary oxygen inlet is chosen to be 1.47 cm.

To mitigate the decreased jet potential core length, the lance inlet must be placed closer to the surface of the bath to ensure that the potential core reaches the surface of the bath. The lance is positioned 30 cm above the surface of the bath, or approximately 10D. In the EAF process, the lance is angled as this increases the mixing in the bath. In this simulation two angles are studied: 30° and 45°. This covers the general operating range of EAF lances, and allows for the comparison of the bath and cavity properties induced from the impinging jet. A dimensioned schematic of the geometry used is shown in Figure 6.2. The green area represents the region of the domain filled with gas, the blue area represents the liquid region, and the lance is shown in red. The bottom and sides of the domain are considered as no-slip walls, the top of the domain is considered a pressure outlet with static pressure 101325 Pa. The properties of the gas and liquid phases are given in Table 6.1.

Phase	Material	Density (kg/m^3)	Dynamic Viscosity (Pa-s)	Surface Tension (N/m)	Temperature (K)
Gas	Air	1.118	1.855E-5	-	298.15
Liquid	Iron	7200	0.006	1.6	298.15

Table 6.1: Properties of the different phases used in the replication of EAF blowing case.

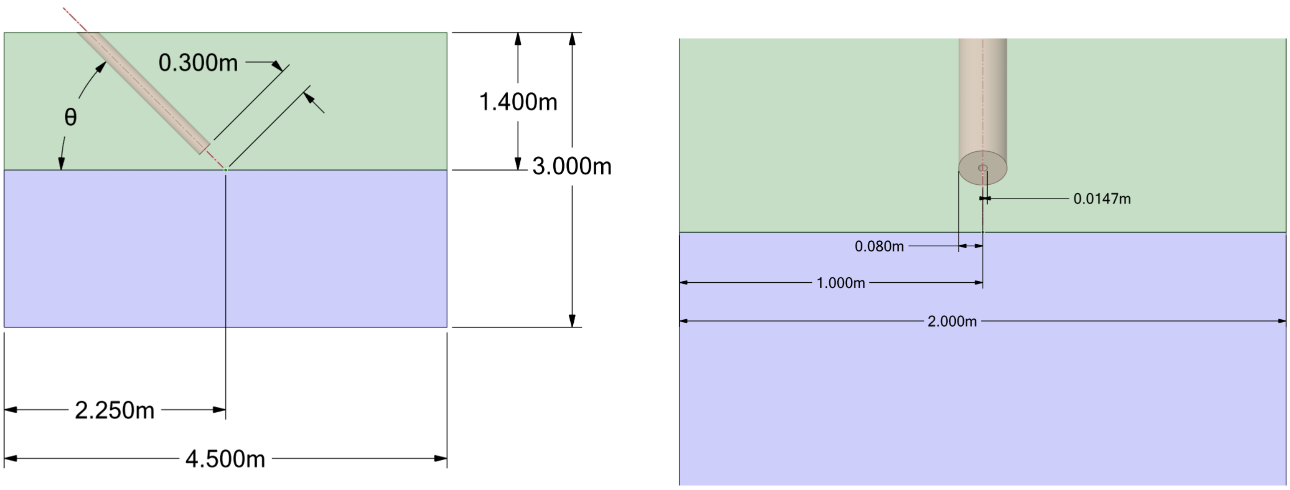

(a) In plane view of angled jet geometry

(b) Zoomed in head on view of angled jet geometry

Figure 6.2: Domain for angled jet simulations

The mesh is constructed in a similar manner to the simplified air-water cases. However, with the elevated velocity of the jet reaching the surface of the bath, the mesh is further refined in the cavity region to enhance stability. To further enhance the stability of the segregated solver for the higher velocity flow, the timestep is reduced to 0.0001 s. The meshes for both lance angles are shown in Figure 6.3. The total mesh element counts are 5726281 cells for the 30° case, and 6166538 cells for the 45° case.

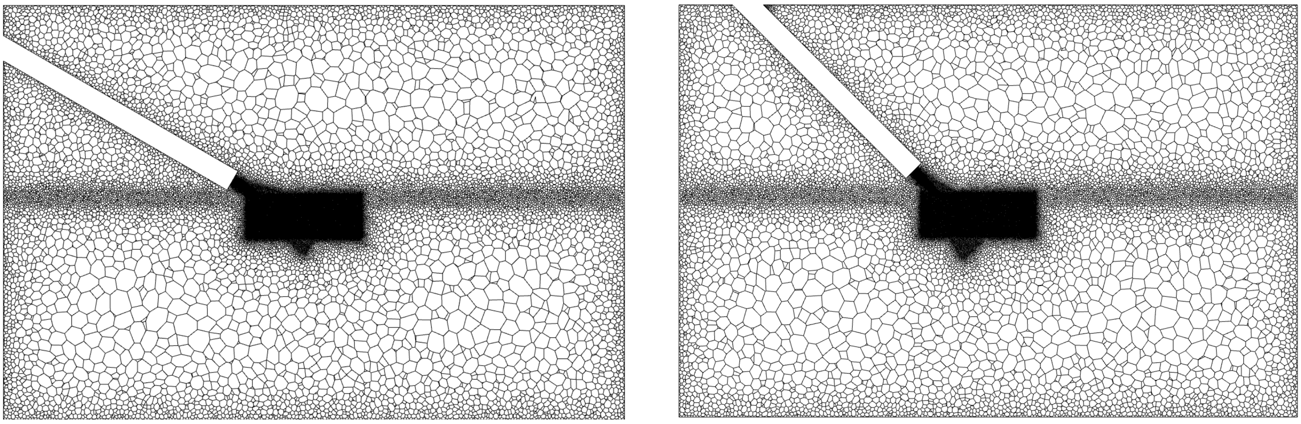

(a) Mesh for 30° case

(b) Mesh for 45° case

Figure 6.3: Jet-Plane cross section view of meshes used for 30° and 45° blowing cases

6.2 Results

To measure the results of the simulation, the inlet pressure is first slowly increased to the final stagnation pressure to ensure stability with the segregated solver. After the inlet is brought up to the correct pressure, and the cavity has reached steady state oscillation the different measurements of the cavity, and flow fields can then be taken.

The first quantity of interest is the centerline velocity with respect to the axial distance from the nozzle. Analyzing the jet velocity as it nears the surface of the bath allows for the assurance that the jet potential core is reaching the bath surface, and thus the results can then be compared to that of the coherent supersonic jet. The jet centerline velocities are shown in Figure 6.4.

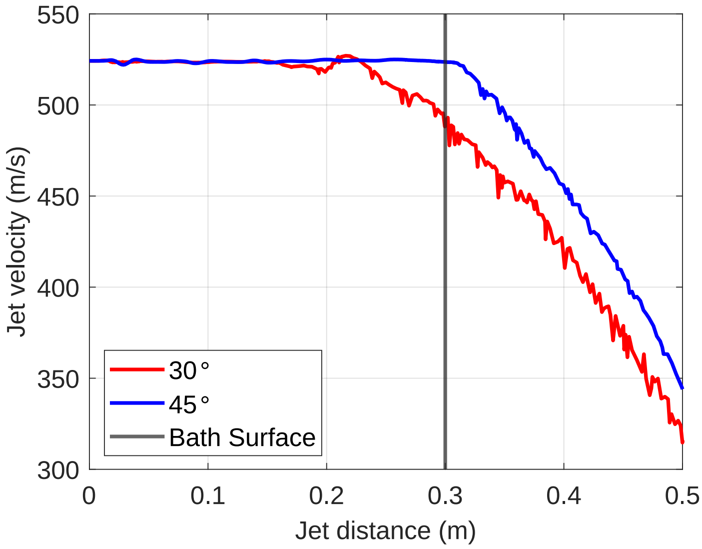

Figure 6.4: Centerline jet velocity comparison with respect to the undeformed surface of the bath

Observing the jet centerline velocities reveals that the potential core velocity is reaching the bath surface in the 45° case, but in the 30° case the velocity starts to diminish before reaching the bath. This can be explained by the difference in cavity depths between the different cases. In the 45° case, the jet impinges at a sharper angle, which imparts more vertical momentum onto the surface of the bath, creating a deeper cavity. This allows the jet to travel further before stagnating upon the surface of the cavity, thus the upstream flow at the surface of the bath will be faster. This can be seen in the cavity depth responses shown in Figure 6.5. The difference between the different mean cavity depths is comparable to that of the difference in jet potential core length showing that the depth of the cavity influences the upstream characteristics of the jet.

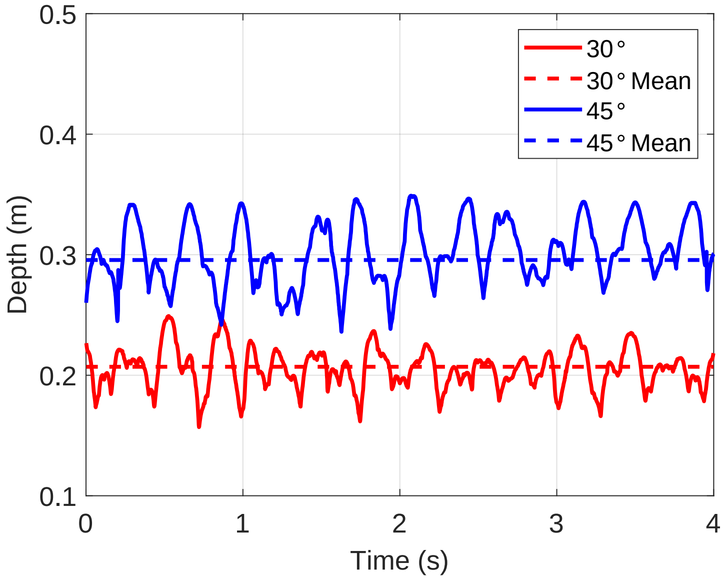

Figure 6.5: Depth Response for the two different angled jets

The different mean cavity depths can also be compared to predicted values from the analytical expressions derived by Alam et al. [14]. The jet momentum is calculated on the inlet surface, while the liquid density, jet height, jet angle, and gravitational constant are all simulation parameters. The value of K_2 is taken to be 7.4. These values are compared in Table 6.2.

Angle	Simulated Depth	Predicted Depth	% Difference
30°	20.70 cm	20.84 cm	-0.67 %
45°	29.56 cm	29.48 cm	0.27 %

Table 6.2: Comparison of simulation cavity depths with analytical expressions.

The simulated depth values for the different lance angles are shown to match well with the analytical expression from Alam et al. [14]. The discrepancy between the simulation results and the experimental correlation is found to be less than 1 % for both cases showing that the analytical expression is accurate for these simplified EAF conditions.

Another quantity of interest is the transient oscillation of the cavity for the angled jet. To analyze this oscillation, FFTs are calculated on the depth responses for the 2 different lance angles. These results are shown in Figure 6.6.

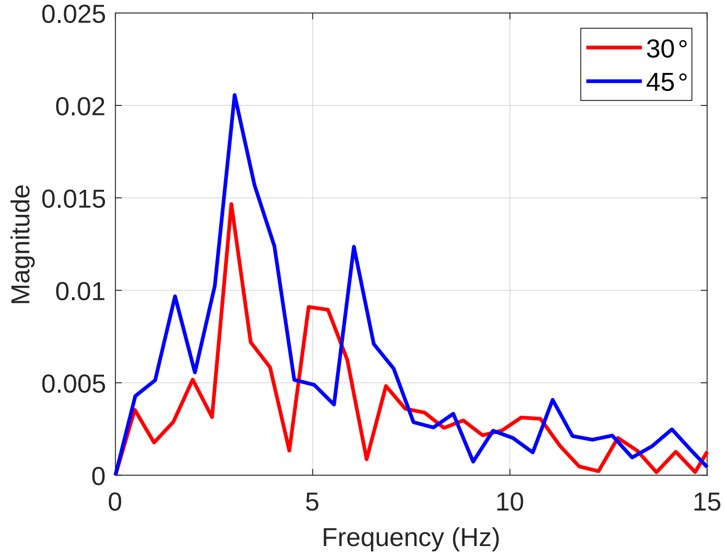

Figure 6.6: FFT Response for the two different angled jets

The cavities for the different cases are found to have similar oscillatory patterns, with a first prominent oscillatory peak at 3.02 Hz for the 45° case, and 2.94 Hz for the 30° case. There is also a second prominent peak for both simulations with frequencies of 6.05 Hz for the 45° case, and a wider peak of 4.90 - 5.39 Hz for the 30° case. Overall, oscillatory cavity response is very similar between the two angled cases, and the frequencies are also comparable to those found for the vertical blowing case. However, these values all differ from those measured in experimental results, which found primary oscillatory frequencies between 4-12 Hz.

To analyze the cavity, and flow induced by the angled impinging jet a different method from the vertically impinging jet must be used due to the asymmetry in the problem. Instead of using radial measurements, two planar sections are positioned perpendicularly across the cavity. The first is positioned streamwise along the jet potential core, the second plane is positioned perpendicular to this plane at the deepest point of the cavity.

To determine the shape of the cavity the volume fraction is measured on these measurement planes for the duration of the steady-state oscillatory solution. This value can then be averaged to yield an average cavity shape. The results for the streamwise, and perpendicular planes for the two different angular cases are shown in Figure 6.7.

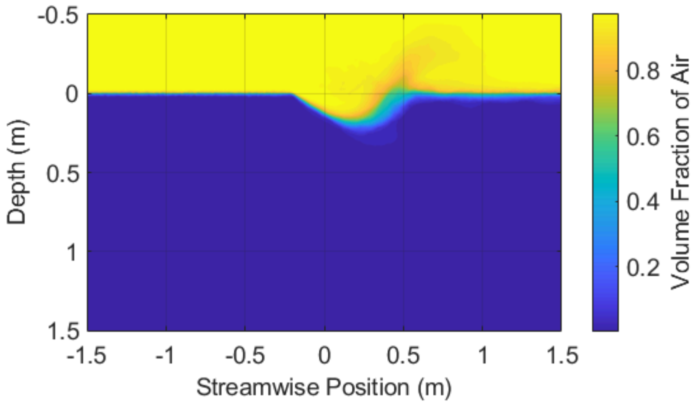

(a) 30° cavity response in plane with jet

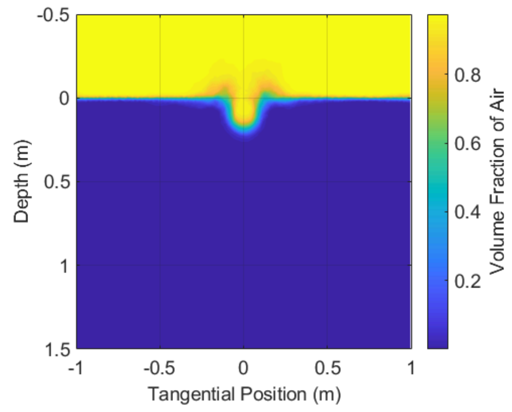

(b) 30° cavity perpendicular to jet

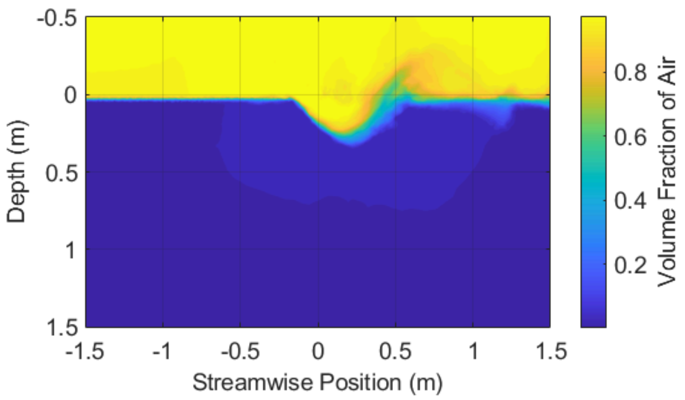

(c) 45° cavity response in plane with jet

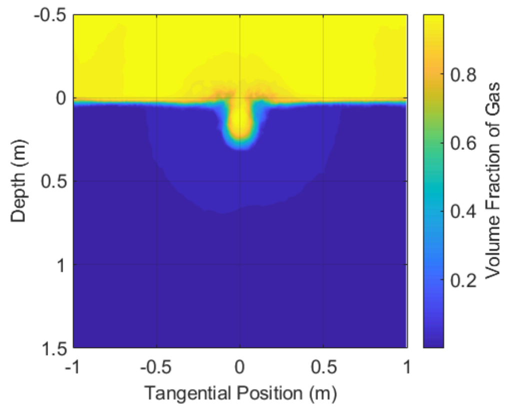

(d) 45° cavity perpendicular to jet

Figure 6.7: Time averaged volume fraction of air for planar cuts in plane with the jet, and perpendicular to the jet in the center of the cavity.

The time average volume fraction shows the interface between the fluids, and the oscillatory region of the cavity located downstream of the stagnation point in the cavity. This shows that unlike the vertically impinging jet, the oscillation of the cavity from the angled jet oscillates primarily along one axis. Analyzing the average volume fraction on the perpendicular plane reveals that the symmetry of the cavity is still maintained across the plane of symmetry of the jet.

The surface of the cavity can then be extracted from the time averaged volume fraction by only plotting the points with a volume fraction of air between 0.49, and 0.51. These cavity shapes on the two measurement planes for the different blowing angles are shown in Figure 6.8.

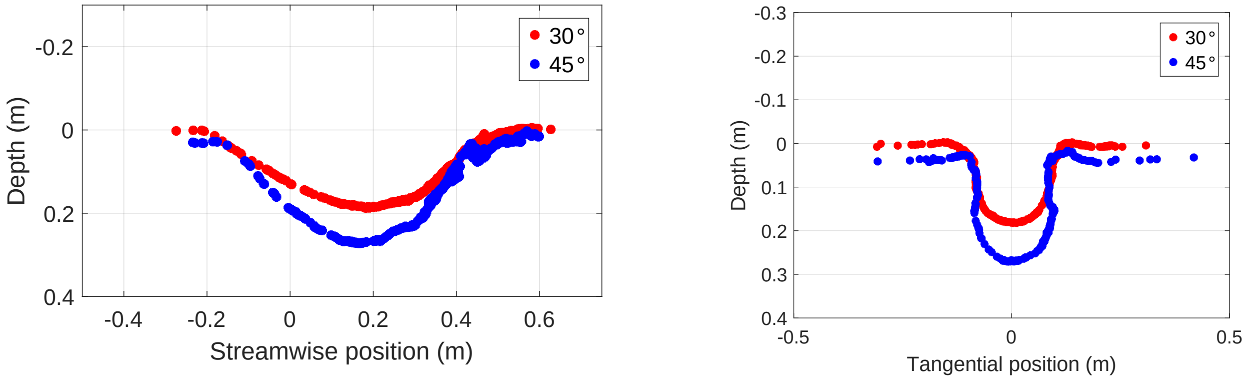

(a) Cavity shape in-plane with centerline of jet (b) Cavity shape normal to the impinging jet

Figure 6.8: Cavity shape comparisons for the different impinging jet angles

The averaged cavity interfaces reveal that the radii of the cavity cross sections for the two different blowing angles is nearly the same, while the depth and shape of the cavity is the main difference. In the 30° case the slope of the cavity is more gradual due to the smaller cavity depth. The radius of the cavity downstream of the impingement point is also found to be much larger than the radius of the cavity upstream of the impingement point. The different cavity radius values are shown in Table 6.3.

	Upstream	Downstream	Tangential
30°	20.68 cm	54.66 cm	12.46 cm
45°	20.83 cm	55.39 cm	12.85 cm

Table 6.3: Table of cavity radius values

Another interesting quantity to note is the average variance in the volume fraction for the different blowing cases. The variance in the volume fraction identifies the regions in the domain in which the cavity is oscillating, which can be used to identify regions with increased mixing. The variance of volume fraction on the different measurement planes is shown in Figure 6.9.

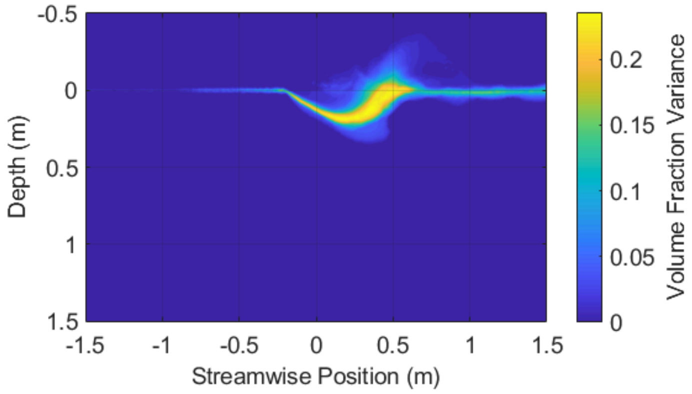

(a) 30° in plane vf variance

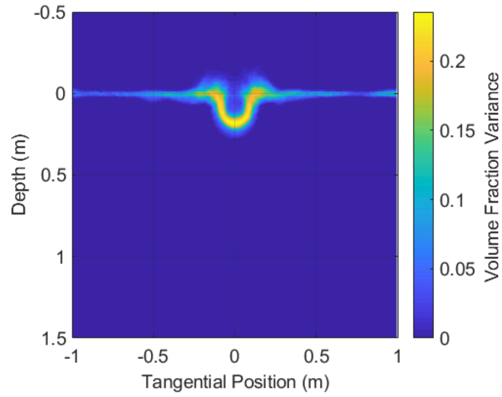

(b) 30° perpendicular vf variance

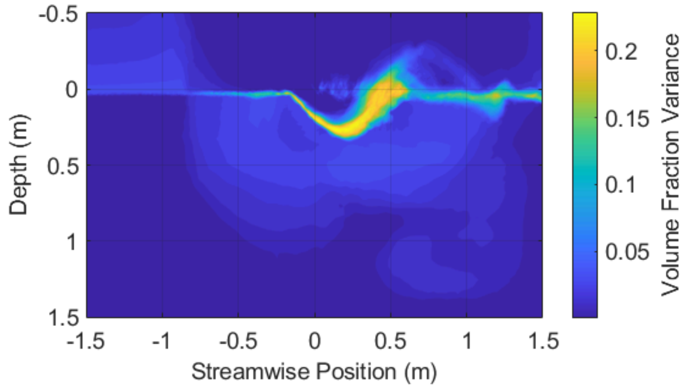

(c) 45° in plane vf variance

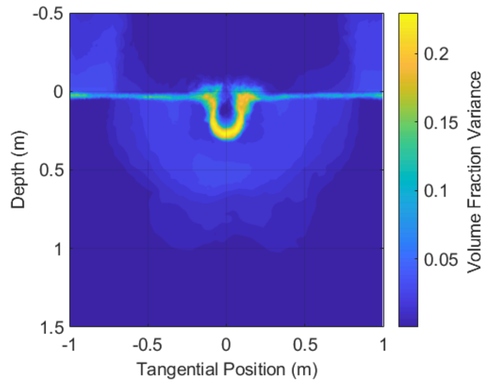

(d) 45° perpendicular vf variance

Figure 6.9: Time averaged variance in volume fraction for planar cuts in plane with the jet, and perpendicular to the jet in the center of the cavity.

The variance in volume fraction is shown to be elevated downstream of the impingement point, where the changing interface is much thicker than the interface upstream of the impingement point. It is also interesting to note the increased interface thickness perpendicular to the jet flow in both cases. The thickness of the downstream region with elevated variance is also found to be larger in the 45° case compared to the 30° case. However, this thickness perpendicular to the jet is found to be similar.

The effects of the cavity oscillation can also be seen downstream of the cavity where there is a region of increased volume fraction variance as a result of splashing, and waves propagated from the cavity. The thickness of the interface in this region is found to be thicker in the 45° due to the higher momentum imparted on the bath.

Another quantity of interest is the velocity field in the bath, this can show which regions around the cavity have increased mixing. Studying the velocity field allows for reaction rate models to be developed to accurately predict species transport in the bath. To determine the region that describes the bath, only the regions with a mean volume fraction of liquid above 0.95 are considered. The velocity fields on the different measurement planes are shown in Figure 6.10

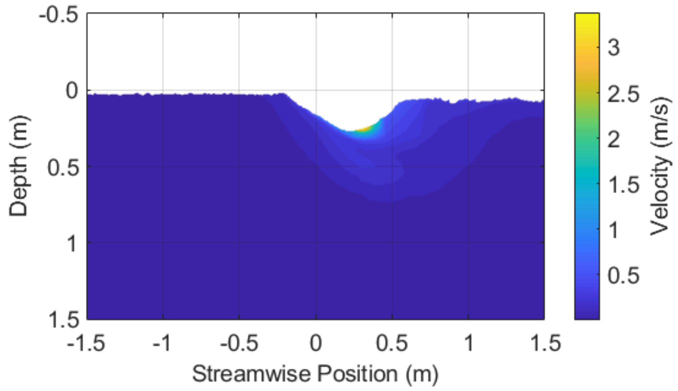

(a) 30° in plane liquid velocity

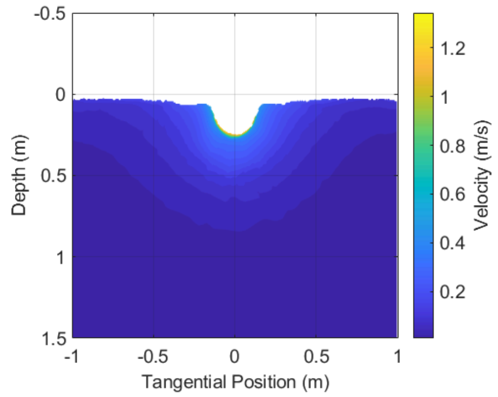

(b) 30° perpendicular liquid velocity

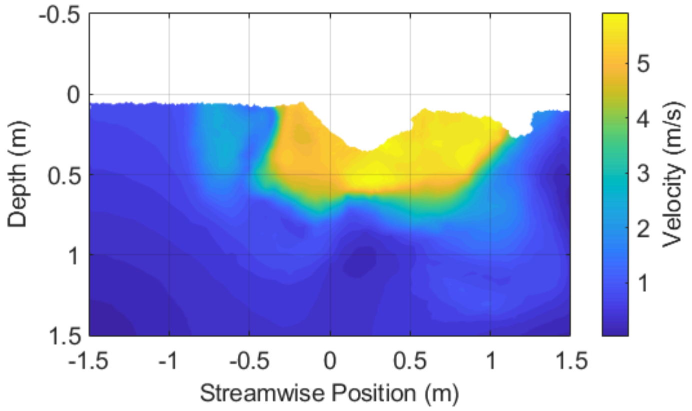

(c) 45° in plane liquid velocity

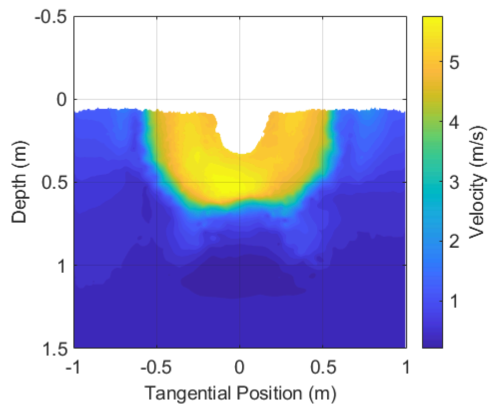

(d) 45° perpendicular liquid velocity

Figure 6.10: Time averaged velocity distribution for planar cuts in plane with the jet, and perpendicular to the jet in the center of the cavity.

The velocity fields in the bath reveals that the average velocity is much higher for the 45° case, with both the axial and perpendicular planes showing higher peak velocities, and larger areas with elevated velocities compared to the 30° case. This can potentially be explained by the wider variation in volume fraction in the cavity formed in the 45° case allowing for more regions around the cavity to measure velocity from the jet, instead of only measuring velocity in the bath. The velocity in both cases shows that the velocity is highest near the surface of the cavity, and it decays as distance to the cavity increases.

This correlation between the high difference in velocity in the regions with high volume fraction variance reveals another interesting quantity to consider, the variance in velocity in the bath. The variance in velocity in the bath can reveal what regions are impacted by the oscillation of the cavity, and what regions are consistently mixed, independent of this oscillation. The standard deviations of the velocities on the different measurement planes are shown in Figure 6.11.

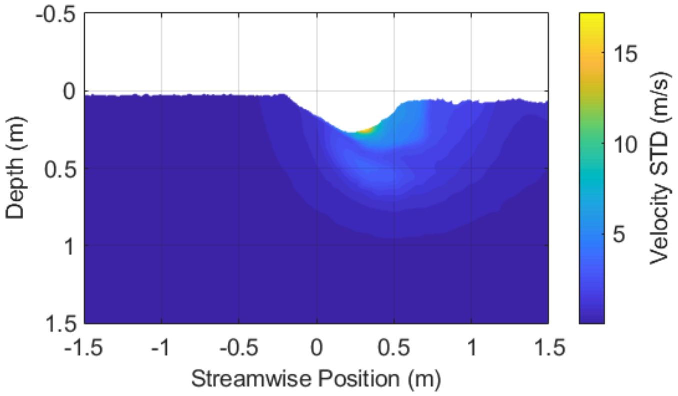

(a) 30° in plane velocity STD

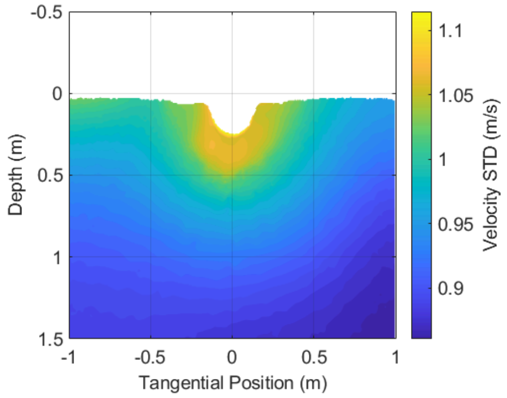

(b) 30° perpendicular velocity STD

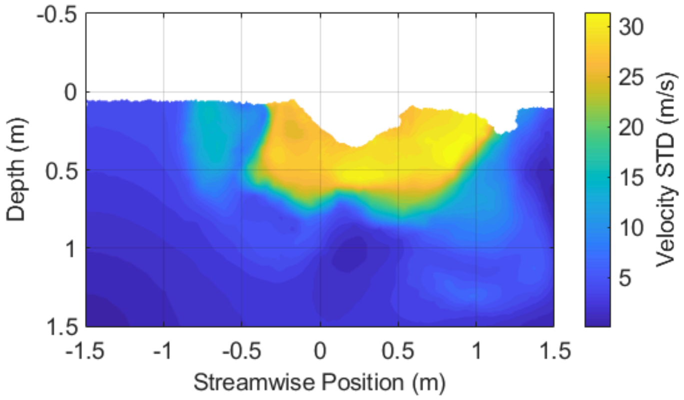

(c) 45° in plane velocity STD

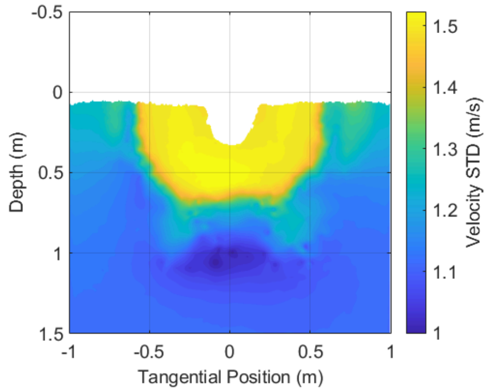

(d) 45° perpendicular velocity STD

Figure 6.11: Time averaged velocity standard deviations for planar cuts in plane with the jet, and perpendicular to the jet in the center of the cavity.

The standard deviation of the velocity is found to be much higher downstream of the impingement point, and much higher in the 45° case compared to the 30° case. The standard deviation of velocity is found to be comparatively low on the perpendicular plane, with the maximum deviation being an order of magnitude lower than the maximum deviation on the axial plane.

Analyzing the regions with elevated standard deviation shows that most of the variance is within 0.5m below the surface for the 30° case, and within 1m below the surface for the 45° case. The high standard deviation of velocity shows an artifact of using the 0.95 volume fraction of liquid cutoff, as air velocity in this region is certainly recorded, influencing the statistics in the near-surface region. However, beneath the surface, the standard deviation distribution shows that upstream of the impingement point there is very little variation in the velocity, while in the downstream region the oscillation of the cavity induces a more variable flow.

To conclude, the cavity created during the EAF process was emulated in a cold model using a standard supersonic jet. To ensure that the jet potential core reached the surface of the bath, the nozzle was positioned roughly 10D above the surface of the bath. The cavity responses were compared for jet angles of 30°, and 45°. It was found that the depth of the cavity was greater in the 45° case, while both results compared well with analytical correlations. It was found that the 45° case created more splashing, and oscillation of the cavity surface in the bath leading to a higher induced velocity in the bath. The variation in volume fraction, and velocity were also studied to determine which regions are influenced by the oscillation of the cavity, and which areas are stable.

Chapter 7

Conclusion

The objective of this thesis was to build towards simulating the EAF process using the VOF method, and determine the limits of the STAR-CCM+ software in conducting this multiphysics problem.

The first step towards simulating the EAF process was to validate the VOF model's accuracy in modeling impinging gas jets onto liquid surfaces. The first validation step consisted of comparing the cavity depth formed from the impinging jet between 2D-axisymmetric and 3D CFD simulations, and experimental correlations. It was found that the cavity depth compared well between the simulations and the experimental correlations, with some discrepancy for lower jet heights. Next the cavity shape was compared between the 2D-axisymmetric and 3D simulations, where it was found that the 2D-axisymmetric cavity shape was not supported by previous literature, while the 3D cavity shape could be approximated by an ellipse. The next step taken to validate the VOF model was to compare the simulated velocity field in the bath with that of an experiment. It was found that the velocity fields in the gas, and liquid phases matched well with the experimental measurements, supporting the VOF method's ability to capture the main bath-flow features induced by an impinging gas jet.

After validating the VOF method, the next step was to build towards emulating the physics found in the EAF process. This was done by emulating the bubbles created by chemical reactions at the cavity surface in the EAF process with Lagrangian bubbles. These Lagrangian bubbles were created at the surface of the cavity, where they were stripped from the gas phase at the cavity interface. The bubbles were created at two different mass fluxes equal to 50% and 100% of the jet mass flow rate. These bubbles were removed according to two different conditions, in the first they were removed one time step after creation, in the second they were removed upon reaching the gas-liquid interface. It was found that the creation of the bubbles slightly increased the depth of the cavity, and decreased the radius of the cavity.

The conditions in the EAF process were then replicated with a cold model and standard supersonic jet. To mitigate the difference in temperature, and lack of flame shroud on the jet core, the jet inlet was positioned closer to the bath such that the potential core reached the surface of the bath. From here the cavity response was measured for jet angles of 30°, and 45°. It was found that the 45° case created a more oscillatory cavity, which induced mixing more than the 30° case. The results of this simplified model can be compared in future work with the cavity response from an impinging coherent jet in EAF ambient conditions.

Future work that can be conducted on this subject includes using the coherent jet in EAF ambient conditions for the angled jet case, introducing slag into the simulation and measuring its impact on the cavity, and adding chemical reactions to compare the resultant cavity shape with those obtained from the Lagrangian bubbles.

Nomenclature

Abbreviations

BF-BOF	Blast Furnace–Basic Oxygen Furnace
BGI	Bottom Gas Injection
CDS	Central-Differencing Scheme
CFD	Computational Fluid Dynamics
CO	Carbon Monoxide
CO_2	Carbon Dioxide
EAF	Electric Arc Furnace
EMS	Electromagnetic Stirring
FFT	Fast Fourier Transform
FVM	Finite Volume Method
RANS	Reynolds-Averaged Navier–Stokes
SIMPLEC	Semi-Implicit Method for Pressure-Linked Equations Consistent
SST	Shear Stress Transport
STP	Standard Temperature and Pressure
VOF	Volume of Fluid

Latin Symbols

a	Cavity depth	m
a_1	Slag-layer thickness	m
a_n^v	Velocity coefficient for neighboring cell n	–
A	Surface area	m^2
b_0	Nozzle width	m
B_*	Empirical constant in cavity-depth correlation	–
C_D	Drag coefficient	–
D	Water or bath depth	m
D_e	Jet exit diameter	m
d_0	Nozzle diameter	m
d_j	Jet diameter	m
f	Linear interpolation factor	–
F	Force	N
g	Gravitational acceleration	m s^{-2}
h	Jet or lance height above the undeformed liquid surface	m
h_g	Slag-layer thickness	m
h_p	Penetration depth	m
H	Nozzle or lance elevation	m
H_0	Initial lance height	m
k	Turbulent kinetic energy	m^2 s^{-2}
K_2	Empirical constant in cavity-depth correlations	–
l	Bubble or particle length scale	m
l_e	Eddy length scale	m
l_t	Turbulent length scale	m
M	Jet momentum	N
M_3	Non-dimensional axisymmetric jet momentum	–
$\dot{m}$	Mass flow rate	kg s^{-1}
n	Time level or index	–
n_0	Cavity depth in the Banks and Chandrasekhara correlation	m
p	Pressure	Pa
p'	Pressure correction	Pa
P	Cavity penetration depth for an angled jet	m
P_0	Stagnation pressure or inlet pressure	Pa
Q	Volumetric flow rate	m^3 s^{-1}
R_j	Nozzle Reynolds number	–
Re_d	Dispersed-phase Reynolds number	–
S_ϕ	Source term for transported variable ϕ	–
t	Time	s
T	Temperature	K
u_c	Axial centerline velocity	m s^{-1}
u_e	Velocity fluctuation standard deviation	m s^{-1}
v	Velocity vector	m s^{-1}
v	Intermediate velocity field	m s^{-1}
v_e	Jet exit velocity	m s^{-1}
v_j	Nozzle or jet velocity	m s^{-1}
v_r	Relative velocity between particle and continuous phase	m s^{-1}
v_x	Jet velocity at axial location x	m s^{-1}
V	Cell volume or control-volume volume	m^3
x	Axial distance from nozzle exit	m
x_{core}	Potential-core length	m

Greek Symbols

α	Volume fraction or empirical jet-spreading coefficient	–
β	Empirical coefficient in potential-core relation	–
γ	Specific weight of liquid	N m^{-3}
γ_L	Specific weight of liquid phase	N m^{-3}
γ_{L1}	Specific weight of slag layer	N m^{-3}
γ_{L2}	Specific weight of bath liquid	N m^{-3}
γ_{Lmix}	Weighted specific weight of two-liquid mixture	N m^{-3}
Γ	Diffusion coefficient	–
Δt	Time step	s
ζ	Non-dimensional cavity diameter	–
θ	Jet angle or outgoing-flow angle	rad or deg
μ	Dynamic viscosity	kg m^{-1} s^{-1}
μ_c	Dynamic viscosity of continuous phase	kg m^{-1} s^{-1}
μ_t	Turbulent dynamic viscosity	kg m^{-1} s^{-1}
ρ	Density	kg m^{-3}
ρ_{amb}	Ambient-gas density	kg m^{-3}
ρ_c	Continuous-phase density or density-based model parameter	kg m^{-3}
ρ_e	Jet exit density	kg m^{-3}
ρ_{out}	Non-dimensional density ratio	–
ρ_x	Jet density at the bath surface	kg m^{-3}
σ	Surface tension	N m^{-1}
τ	Jet thrust or characteristic time scale, depending on context	N or s
τ_c	Particle crossing time scale	s
τ_e	Eddy time scale	s
τ_I	Particle–eddy interaction time	s
τ_t	Turbulent time scale	s
ϕ	Generic transported scalar	–
ω	Specific weight of liquid or specific dissipation rate, depending on context	N m^{-3} or s^{-1}

Bibliography

[1] Charter Steel, "Eaf vs. bof furnaces in steelmaking," 2024. Accessed: 2026-05-12.

[2] M. Sporchia, "Electric steelmaking – the processing route." SlideShare presentation, 2019. Accessed: 2026-05-12.

[3] A. N. Conejo and Z. Yan, "Electric arc furnace stirring: A review," *Steel Research International*, vol. 94, no. 7, p. 2200864, 2023.

[4] J. von Schéele, H. Alshawarghi, P. Kwaschny, H. Groiss, J. van Lingen, and D. Razzari, "Energy-efficient and hydrogen-ready technologies for eaf steelmaking," *La Metallurgia Italiana*, pp. 52–63, Mar. 2024.

[5] G. Tang, Y. Chen, A. K. Silaen, Y. Krotov, M. F. Riley, and C. Q. Zhou, "Effects of fuel input on coherent jet length at various ambient temperatures," *Applied Thermal Engineering*, 2019.

[6] N. Molloy, "Impinging jet flow in a 2-phase system-basic flow pattern," *Journal of the iron and steel institute*, vol. 208, p. 943, 1970.

[7] M. V. Ende, "Development of an electric arc furnace simulation model using the effective equilibrium reaction zone (eerz) approach," *JOM*, vol. 74, pp. 1610–1623, feb 2022.

[8] O. Haile and L. Holappa, "Current status of converter steelmaking," tech. rep., Helsinki University of Technology, Espoo, Finland, 1995.

[9] F. R. Cheslak, J. A. Nicholls, and M. Sichel, "Cavities formed on liquid surfaces by impinging gaseous jets," *Journal of Fluid Mechanics*, vol. 36, pp. 55–63, mar 1969.

[10] R. B. Banks and D. V. Chandrasekhara, "Experimental investigation of the penetration of a high-velocity gas jet through a liquid surface," *Journal of Fluid Mechanics*, vol. 15, pp. 13–34, jan 1963.

[11] M. Alam, J. Naser, and G. Brooks, "Computational fluid dynamics simulation of supersonic oxygen jet behavior at steelmaking temperature," *Metallurgical and Materials Transactions B*, vol. 41B, no. 3, pp. 636–645, 2010.

[12] I. Sumi, Y. Kishimoto, Y. Kikuchi, and H. Igarashi, "Effect of high-temperature field on supersonic oxygen jet behavior," *ISIJ International*, vol. 46, no. 9, pp. 1312–1317, 2006.

[13] F. Qian, R. Mutharasan, and B. Farouk, "Studies of interface deformations in single- and multi-layered liquid baths due to an impinging gas jet," *Metallurgical and Materials Transactions B*, vol. 27B, no. 6, pp. 911–920, 1996.

[14] M. Alam, G. Irons, G. Brooks, A. Fontana, and J. Naser, "Inclined jetting and splashing in electric arc furnace steelmaking," *ISIJ International*, vol. 51, no. 9, pp. 1439–1447, 2011.

[15] M. S. Lee, S. L. O'Rourke, and N. A. Molloy, "Oscillatory flow in the steelmaking vessel," *Scandinavian Journal of Metallurgy*, vol. 32, no. 5, pp. 281–288, 2003.

[16] R. Berger, S. Depardon, P. Rambaud, and J. M. Buchlin, "Experimental investigation of a 2d impinging jet on a liquid surface," in *Computational Methods in Multiphase Flow V*, vol. 63 of *WIT Transactions on Engineering Sciences*, pp. 507–518, WIT Press, 2009.

[17] G. Tang, Y. Chen, A. K. Silaen, Y. Krotov, M. F. Riley, and C. Q. Zhou, "Investigation on coherent jet potential core length in an electric arc furnace," *steel research international*, vol. 90, p. 1800381, 2019.

[18] World Steel Association, "What is steel?," 2026. Accessed: 2026-05-12.

[19] Oxford Economics, "The role of steel manufacturing in the global economy," tech. rep., World Steel Association, May 2019. Accessed: 2026-05-12.

[20] World Steel Association, "World steel in figures 2025," tech. rep., World Steel Association, 2025. Accessed: 2026-05-12.

[21] Nucor Corporation, "How to make steel: Blast furnace vs. electric arc furnace," 2024. Accessed: 2026-05-12.

[22] European Steel Association (EUROFER), "What is steel and how is steel made," 2025. Accessed: 2026-05-12.

[23] R. Singh, "Production of steel," in *Applied Welding Engineering: Processes, Codes, and Standards*, ch. 5, pp. 33–50, Elsevier, 2012.

[24] P. C. Mathur, W. J. Mahoney, S. K. Warty, and J. von Schéele, "Coherent jets in steelmaking: Principles and learnings," in *AISTech Conference Proceedings*, Association for Iron & Steel Technology, 2006.

[25] D. H. Wakelin, *The Interaction Between Gas Jets and the Surfaces of Liquids, Including Molten Metals*. Phd thesis, University of London, London, United Kingdom, 1966.

[26] M. Evestedt and A. Medvedev, "Cavity depth and diameter estimation in the converter process water model," in *Proceedings of the ASME 1997 International Mechanical Engineering Congress and Exposition*, ASME International Mechanical Engineering Congress and Exposition, Proceedings (IMECE), (Dallas, Texas, USA), pp. 43–50, American Society of Mechanical Engineers (ASME), 1997.

[27] S. Ito and I. Muchi, "Transport phenomena of supersonic jet in oxygen top blowing converter," *Tetsu-to-Hagane*, vol. 55, no. 13, pp. 1152–1163, 1969.

[28] G. Wei, R. Zhu, T. Cheng, K. Dong, and R. Liu, "Modelling on the penetration depth of the coherent supersonic jet in eaf steelmaking," *Ironmaking & Steelmaking*, vol. 45, no. 9, pp. 828–838, 2018.

[29] R. D. Collins and H. Lubanska, "The depression of liquid surfaces by gas jets," *British Journal of Applied Physics*, vol. 5, no. 1, pp. 22–28, 1954.

[30] H. Y. Hwang and G. A. Irons, "Mathematical modeling of impinging gas jets on liquid surfaces," *Metallurgical and Materials Transactions B*, vol. 42B, no. 3, pp. 575–591, 2011.

[31] A. Chatterjee and B. A. C., "Breakup of a liquid surface by an impinging gas jet," *Journal of the Iron and Steel Institute*, vol. 210, p. 179, 1972.

[32] M. Adib, M. A. Ehteram, and H. Basirat Tabrizi, "Numerical and experimental study of oscillatory behavior of liquid surface agitated by high-speed gas jet," *Applied Mathematical Modelling*, vol. 62, pp. 249–266, 2018.

[33] M. Lee, V. Whitney, and N. Molloy, "Jet-liquid interaction in a steelmaking electric arc furnace," *Scandinavian Journal of Metallurgy*, vol. 30, no. 5, pp. 330–336, 2001.

[34] L. Schiller and A. Naumann, "Über die grundlegenden berechnungen bei der schwerkraftaufbereitung," *Zeitschrift des Vereines Deutscher Ingenieure*, vol. 77, no. 12, pp. 318–320, 1933.

[35] Y. Chen, *Integrated Multi-Physics Modeling of Steelmaking Process in Electric Arc Furnace*. Ph.d. dissertation, Purdue University, West Lafayette, Indiana, Aug. 2022.